JACS
JOURNAL OF THE AMERICAN CHEMICAL SOCIETY
pubs.acs.org/JACS
Article

# Pulsed Multifrequency Electron Paramagnetic Resonance Spectroscopy Reveals Key Branch Points for One- vs Two-Electron Reactivity in Mn/Fe Proteins

Effie C. Kisgeropoulos,[‖] Yunqiao J. Gan,[‖] Samuel M. Greer, Joseph M. Hazel, and Hannah S. Shafaat*

Cite This: *J. Am. Chem. Soc.* 2022, 144, 11991−12006
Read Online
ACCESS | Metrics & More | Article Recommendations | Supporting Information

**ABSTRACT:** Traditionally, the ferritin-like superfamily of proteins was thought to exclusively use a diiron active site in catalyzing a diverse array of oxygen-dependent reactions. In recent years, novel redox-active cofactors featuring heterobimetallic Mn/Fe active sites have been discovered in both the radical-generating R2 subunit of class Ic (R2c) ribonucleotide reductases (RNRs) and the related R2-like ligand-binding oxidases (R2lox). However, the protein-specific factors that differentiate the radical reactivity of R2c from the C−H activation reactions of R2lox remain unknown. In this work, multifrequency pulsed electron paramagnetic resonance (EPR) spectroscopy and ligand hyperfine techniques in conjunction with broken-symmetry density functional theory calculations are used to characterize the molecular and electronic structures of two EPR-active intermediates trapped during aerobic assembly of the R2lox Mn/Fe cofactor. A $Mn^{III}(\mu\text{-}O)(\mu\text{-}OH)Fe^{III}$ species is identified as the first EPR-active species and represents a common state between the two classes of redox-active Mn/Fe proteins. The species downstream from the $Mn^{III}(\mu\text{-}O)(\mu\text{-}OH)Fe^{III}$ state exhibits unique EPR properties, including unprecedented spectral breadth and isotope-dependent g-tensors, which are attributed to a weakly coupled, hydrogen-bonded $Mn^{III}(\mu\text{-}OH)Fe^{III}$ species. This final intermediate precedes formation of the $Mn^{III}/Fe^{III}$ resting state and is suggested to be relevant to understanding the endogenous reactivity of R2lox.

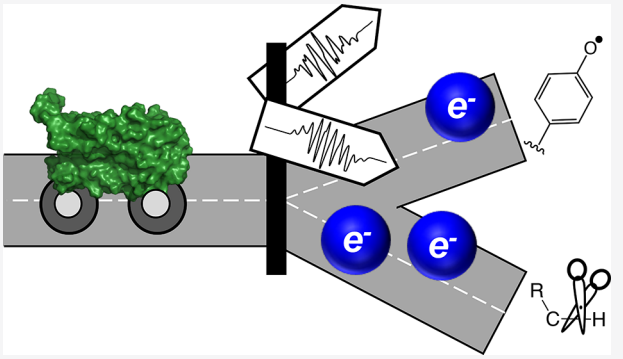


## INTRODUCTION

The ferritin-like superfamily of proteins is found across all three kingdoms of life, critical for catalyzing a diverse array of reactions ranging from iron storage and oxygen transport, to hydrocarbon oxidation and radical initiation, to antibiotic biosynthesis.[1−3] Typically, these proteins feature a carboxylate-rich diiron core and utilize oxygen as a co-substrate, reducing it to water during catalysis. However, characterization of emergent members of this superfamily calls into question the universality of both the cofactor and catalyzed chemical processes. For example, redox-neutral deformylation has been established as the mechanism behind alkane formation by the ferritin-like aldehyde deformylating oxidase proteins in cyanobacteria,[4,5] and cofactors featuring heterobimetallic Mn/Fe active sites have been discovered in both the radical-generating R2 subunit of class Ic (R2c) ribonucleotide reductases (RNRs)[6,7] and the related R2-like ligand-binding oxidase (R2lox).[8,9] As the sequences of increasingly diverse microorganisms become available, additional functional variation across this superfamily is anticipated, with corresponding questions about structure−function relationships. Understanding the protein-derived elements and metallocofactor distinctions that contribute to divergent reactivity represents a critical area of research in this field.

The two redox-active Mn/Fe proteins identified thus far, the R2c and R2lox proteins, both spontaneously and selectively form a Mn/Fe cofactor *in vitro*, going against the commonly accepted Irving−Williams series for metal-binding affinities.[9−13] However, upon oxygen activation, the chemistry performed by the two proteins is quite distinct. The R2c protein proceeds through a high-valence, $Mn^{IV}/Fe^{IV}$ intermediate before abstracting an electron from an unknown source to arrive at the $Mn^{IV}/Fe^{III}$ resting state.[14−16] This $Mn^{IV}/Fe^{III}$ cofactor initiates reversible, long-range proton-coupled electron transfer, resulting in a quasi-stable $Mn^{III}/Fe^{III}$ species, and the protein simply cycles between those one-electron redox transitions during turnover.[15,17] R2lox, on the other hand, catalyzes a net C−H bond oxidation reaction upon

**Received:** December 31, 2021
**Published:** July 5, 2022






https://doi.org/10.1021/jacs.1c13738
*J. Am. Chem. Soc.* 2022, 144, 11991−12006

$O_2$ activation of the metallocofactor to generate an unprecedented tyrosine-valine cross-link within its scaffold (Figure 1), carrying out a selective two-electron oxidation

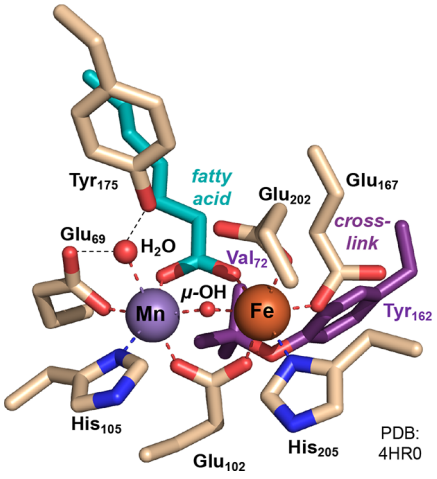


**Figure 1.** Active site of Mn/Fe WT R2lox. Residues in primary and secondary coordination spheres are indicated. Hydrogen bonding interactions are shown between the Mn-bound water ligand and E69 and Y175 (black, dashed lines).

reaction that bypasses the "radical rebound" process commonly seen in hydrocarbon oxygenases.[9,12,18−21] Neither the R2c nor the R2lox protein support the same reactivity in the absence of Mn.[6,11,22] While both proteins can assemble the canonical Fe/Fe cofactor, R2c can only support a single-turnover process due to the high reduction potential of the $Fe^{IV}/Fe^{III}$ state, and cross-link formation in R2lox is significantly more efficient in the Mn/Fe cofactor.[11,12,18,21] R2lox thus represents the first example of a biological Mn/Fe system known to access multielectron chemistry.[1,6,9,23,24]

Mössbauer spectroscopy has been used extensively to resolve the structures of intermediates in the diiron proteins, allowing detailed correlations to be drawn between enzymatic intermediates and well-defined model compounds.[1] Historically, electron paramagnetic resonance (EPR) spectroscopy has often been used as a complement to Mössbauer spectroscopy, especially to study exchange coupling and the nature of spin-coupled, mixed-valence metal clusters. Early work on diiron clusters in systems such as the class Ia RNR, methane monooxygenase, and others used cryoreduction to generate the mixed-valence $Fe^{II}/Fe^{III}$ cluster from the EPR-silent, diferric resting state.[25−28] Such experiments resolved hyperfine and exchange coupling values and provided a foundational understanding of the electronic structure of dimetal clusters. EPR spectroscopy is also an ideal technique for characterization of the homovalent states of Mn/Fe proteins, offering sensitivity, selectivity, and detailed structural and electronic information.[29] The bridging ligand(s) between the metals generally mediate(s) antiferromagnetic exchange, leading to an $S = {}^1/_2$ total ground spin state that is easily probed using conventional EPR techniques. The spectral features reflect the projection of the individual metal ions onto the coupled system[30] and are highly sensitive to the exchange interaction between the metals, to the extent that mutations modifying the outer-sphere hydrogen bonding network have been shown to affect the observed resting-state spectrum.[11] Such remote perturbations are rarely resolved in continuous-wave (CW) EPR spectroscopy and highlight the opportunity for pulsed EPR to provide high-resolution characterization of metalloprotein active sites.[31]

The final resting state (RS) of the R2lox cofactor has a well-characterized, spin-coupled $Mn^{III}(\mu\text{-OH})Fe^{III}$ center.[20] A mechanism for $O_2$ activation and cross-link formation had been proposed on the basis of initial kinetic analysis and through homology to related diiron proteins;[32] however, the structures of the relevant catalytic intermediates remain undetermined. In this work, we apply CW and pulsed EPR techniques at X- (9.4 GHz), Q- (34 GHz), and W-band (94 GHz) frequencies to resolve the geometric and electronic structures of two of the transient Mn/Fe intermediates observed upon aerobic metalation and $O_2$ activation of R2lox. Decomposition of the coupled spectra gives the intrinsic properties of each metal center, revealing the local distortion of the $Mn^{III}$ site, and hyperfine techniques are used to probe ligand interactions. The sensitivity of the EPR spectrum to local properties is further illustrated by changes induced through H/D isotopic substitution, which are attributed to modulation of the exchange coupling due to differential hydrogen bonding across the isotopes (*vide infra*). Broken symmetry density functional theory (DFT) calculations complement the experimental work to provide refined structural models of the two intermediate species.

Resolving the structures of R2lox intermediates that are generated upon $O_2$ activation can shed light on putative physiological substrates and metabolic roles of the protein. Such questions are important because R2lox has been identified as a key virulence factor for *Mycobacterium tuberculosis*, with homologs identified in numerous pathogenic bacteria and extremophilic archaea.[33,34] Establishing the ability of Mn to replace Fe for catalyzing potent C−H bond activation processes thus has implications for understanding how such organisms may circumvent Fe limitations, which is a leading host immune response in, for example, tuberculosis infections.[35,36] Ultimately, establishing structure−reactivity−function relationships in R2lox will provide insight into the chemical capacity of this novel metallocofactor, contributing to our understanding and identification of naturally occurring Mn/Fe proteins.

## RESULTS

### Freeze-Quenched WT R2lox Assembly Intermediates $I_3$ and $I_4$ Show Distinct Kinetics and Spectral Properties.

Two EPR-active, spin-coupled Mn/Fe species were previously identified during aerobic R2lox assembly, each with distinct spectroscopic features and relaxation properties. Based on the kinetic profiles (Figure 2, inset), the first EPR-active species to appear and decay had been tentatively attributed to the species with an optical band at 620 nm, which also forms and decays rapidly. Further resolution of the EPR properties as well as comparison to a trapped species in the G68L mutant of R2lox has inspired us to revisit this assignment, leading us to suggest that the first two optically active intermediates, $I_1$ and $I_2$, cannot be observed using EPR spectroscopy under the present reaction conditions due to limited accumulation.[32,37] To characterize the first intermediate species observed in EPR, $I_3$, samples were prepared with either $^{NA}Fe$ or $^{57}Fe$ in a 0.5:0.5:1 (Mn:Fe:apo-R2lox) ratio and quenched at approx. 45 s (Figure 2). Spectral simulations reveal a spin-coupled, near-axial system with the unique axes of both the $^{55}Mn$ and $^{57}Fe$ metal hyperfine (A) tensors rotated with respect to the g-


https://doi.org/10.1021/jacs.1c13738
J. Am. Chem. Soc. 2022, 144, 11991−12006

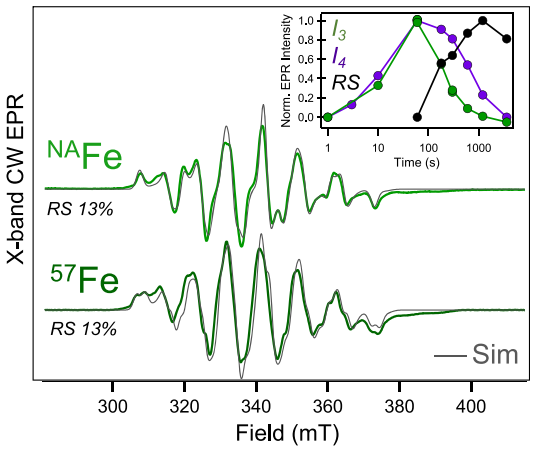


**Figure 2.** X-band CW EPR spectra of the WT R2lox $I_3$ species ($T$ = 30 K; $P$ = 0.2 mW). The $I_3$ intermediate was generated using either $^{NA}$Fe (light green) or $^{57}$Fe (dark green) and quenched at approx. 45 s. Spin Hamiltonian simulations are overlaid (gray) with parameters given in Table 1; the percent contribution from the resting state (RS) to each spectrum was determined by a multicomponent simulation. (Inset) Normalized intensity profiles of $I_3$ and $I_4$ compared to that of the RS as a function of time.

tensor (Table 1). The SH parameters are similar to those of the reduced state of R2c and nearly identical to those reported for the G68L R2lox species (Figure 2 and Table 1).[6,37,38] This species is noted to saturate easily, indicative of a well-isolated ground state, and could not be analyzed using a fit to the Curie law because of saturation effects (Figure S1). Temperature-dependent power saturation studies suggest an energy spacing ($\Delta$) of $\sim -120$ cm$^{-1}$ between the ground and first excited state, corresponding to an exchange coupling constant ($J$) of $\sim -40$ cm$^{-1}$ (Figure S2).[39]

Taking advantage of the distinct relaxation properties, the $I_3$ species can be saturated at low temperatures and high powers. This procedure isolates an exceptionally broad CW EPR signal with a nine-line splitting pattern, attributed to a species designated $I_4$ (Figure 3A). To visualize the contributions that each component makes to the overall spectrum, the simulation is decomposed along each of the principal components (Figure 3B), revealing the pronounced anisotropy of the g- and hyperfine (A) tensors. The simulated powder EPR spectrum of the $I_4$ species without any contribution from hyperfine interactions is shown in the black trace. The three turning points ($g$-values) that describe the three principal axes of the molecular frame display a classic rhombic powder pattern. The additional splitting of the spectrum when accounting for hyperfine structure (colored traces) is a result of anisotropic coupling to $^{55}$Mn and/or $^{57}$Fe. Each of the three principal axes in the black trace is split into six evenly spaced lines due to the hyperfine interaction from $^{55}$Mn (I = 5/2), with additional hyperfine structure from $^{57}$Fe (I = 1/2). The sum of the hyperfine pattern combined with the indicated resting state contribution produced the experimental spectra shown in Figure 3.

**Multifrequency, Pulsed EPR Confirms a Substantial Degree of g-Tensor Anisotropy in $I_4$.** A multifrequency, pulsed EPR approach was employed to separate the Zeeman and hyperfine interactions and fully characterize the spin Hamiltonian parameters of the $I_4$ species (Figure 3C,D). While CW Q-band experiments were initially attempted, rapid passage effects prevented straightforward analysis,[40] most likely due to the contributions from the residual $Mn^{II}$ present in these freeze-quenched intermediate samples. The use of pulsed techniques, however, resolved the underlying intermediate spectrum. While the slower relaxation of both $Mn^{II}$ and $I_3$ allows them to be easily saturated in CW EPR at low temperatures (i.e., 5 K), the use of relaxation alone to separate distinct species is more complicated in pulsed EPR, where both longitudinal ($T_1$) and transverse ($T_2$) relaxation rates contribute significantly to modulate spin echo intensity.[41] Attempts to disentangle multiple species from one another using the relaxation filtering approach (REFINE) resulted in prohibitively low signal intensities (Figure S3).[42,43] Instead, by using higher powers, contributions from contaminating $Mn^{II}$

**Table 1. Projected Spin Hamiltonian Parameters Describing Intermediate Species in WT R2lox**

| | | | | | | | | $Mn^{III}$ | | | | | $Fe^{III}$ | | | | |
|---|---|---|---|---|---|---|---|---|---|---|---|---|---|---|---|---|---|
| | | J (cm$^{-1}$)[a] | $g_1$ | $g_2$ | $g_3$ | $g_{iso}$[b] | $g_{aniso}$[c] | $A_1$ | $A_2$ | $A_3$ | $A_{iso}$ | $A_{aniso}$ | $A_1$ | $A_2$ | $A_3$ | $A_{iso}$ | $A_{aniso}$ |
| $I_3$[d] | $H_2O$ | −40 | 2.034 ± 0.004[e] | 2.026 ± 0.012 | 2.004 ± 0.006 | 2.021 | 0.0026 | 279 ± 10 | 362 ± 8 | 241 ± 20 | 294 | 102 | 66 | 65 | 54 | 62 | 12 |
| $I_4$ | $H_2O$ | −15 to −3 | 2.0605 ± 0.002 | 1.959 ± 0.006 | 1.865 ± 0.016 | 1.962 | 0.149 | 323 ± 12 | 328 ± 15 | 237 ± 16 | 296 | −88.5 | 89[f] | 70 | 76 | 78 | 16 |
| | $D_2O$ | − | 2.059 | 1.958 | 1.854 | 1.957 | 0.153 | 335 | 342 | 238 | 305 | −100.5 | | | | | |
| RS | $H_2O$ | −8 to −1.8 | 2.034 | 1.968 | 1.953 | 1.985 | 0.074 | 282 | 249 | 257 | 263 | 29.3 | 94[f] | 52 | 62 | 69 | 37 |
| | $D_2O$ | − | 2.032 | 1.965 | 1.951 | 1.983 | 0.074 | 286 | 244 | 257 | 262 | 35.5 | | | | | |

[a]Exchange coupling $J$ extracted from temperature-dependent relaxation studies on samples prepared in $H_2O$. [b]The isotropic g- and A- terms are given as averages of the individual values: $g_{iso} = (g_1 + g_2 + g_3)/3$ and $A_{iso} = (A_1 + A_2 + A_3)/3$. [c]The anisotropy in the g- and A-tensors is expressed as the difference between the unique component ($g_z$, $A_z$) and the average of the other two components: $g_{aniso} = g_z - (g_x + g_y)/2$ and $A_{aniso} = A_z - (A_x + A_y)/2$. [d]The $I_3$ $^{55}$Mn hyperfine tensor is rotated with respect to the g-tensor by the Euler angles $[\alpha\ \beta\ \gamma] = [-80°, 69°, 42°]$. [e]Description of error analysis given in Materials and Methods. [f]The $^{57}$Fe coupling was not sufficiently resolved to extract isotope-dependent A-tensor values. Given values are rounded to the nearest integer. The resting state $^{57}$Fe A-tensor is taken from ref 20.



https://doi.org/10.1021/jacs.1c13738
J. Am. Chem. Soc. 2022, 144, 11991−12006

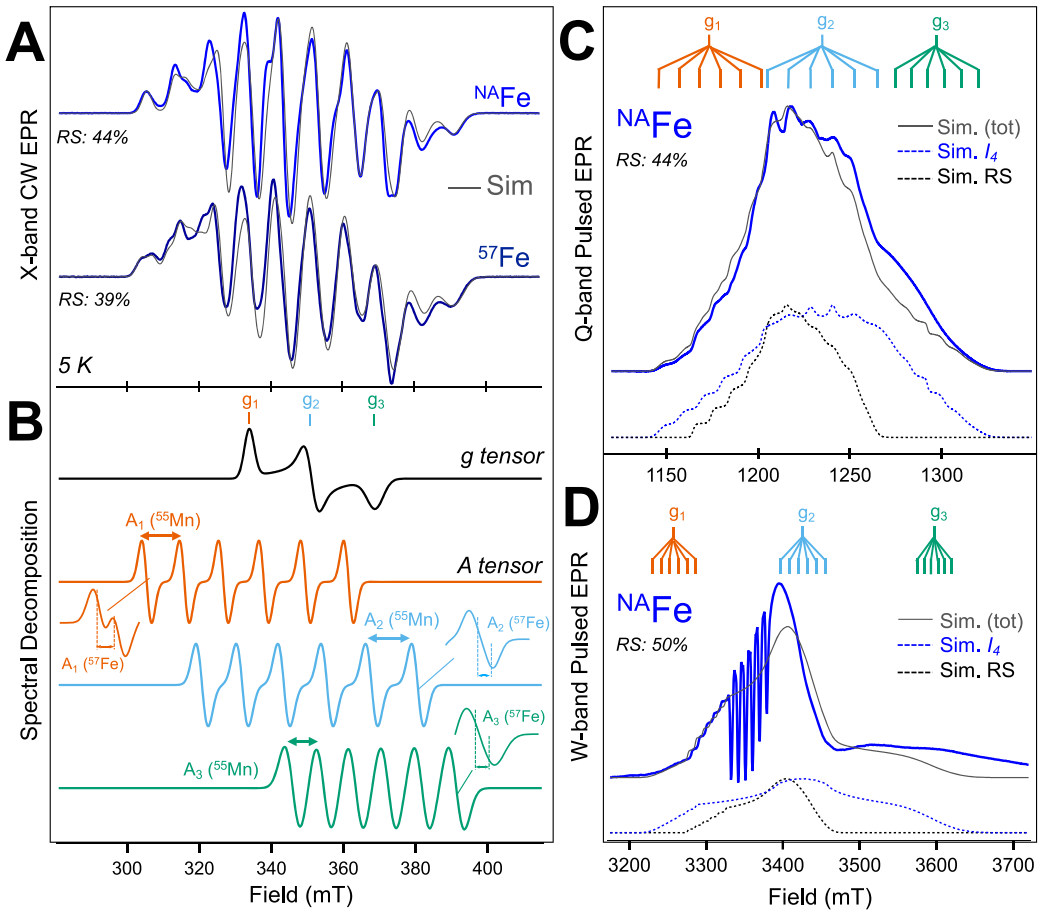


**Figure 3.** Multifrequency EPR spectra of the WT $I_4$ species generated using either $^{NA}$Fe (light blue) or $^{57}$Fe (dark blue) and quenched at ~45 s. SH simulations using parameters given in Table 1 are overlaid (gray); the contribution from the resting state (RS) to each spectrum was determined by a multicomponent simulation. (A) X-band CW EPR spectra ($T$ = 5 K; $P$ = 20 mW) of the WT $I_4$ species. (B) Decomposition of the $I_4$ spectrum based on projected SH parameters obtained from multifrequency simulations. The top, black trace shows the projected g-tensor of the metallocofactor. Lower, colored traces show the effect of the $^{55}$Mn hyperfine structure along each turning point, with additional structure due to $^{57}$Fe shown as insets. (C) Pulsed Q-band ($t_\pi$ = 24 ns; $\tau$ = 200 ns) and (D) W-band ($t_\pi$ = 200 ns; $\tau$ = 850 ns) EPR spectra of the WT $I_4$ species; dotted lines represent the simulated $I_4$ (blue) and RS (black) species.

can be suppressed through overrotation of the S = 5/2 signal (Figure S4). This approach greatly reduces the broad $Mn^{II}$ signal, allowing the signal from the $I_4$ species to be more clearly resolved.

Global simulations of the multifrequency data were performed to obtain a single set of spin Hamiltonian parameters in the projected basis that reproduce the spectral features of the $I_4$ species (Table 1). Microwave nutations were used to confirm the ground spin state of $I_4$ as $S_T = {}^1/_2$ (Figure S5). The g-tensor is almost fully rhombic, unlike the near-axial g-tensors seen in the RS and $I_3$ species. The $^{55}$Mn and $^{57}$Fe hyperfine tensors are both approximately axial but have distinct unique axes; the $^{55}$Mn unique axis is aligned along $g_3$, while the $^{57}$Fe unique axis is aligned along $g_1$. In addition, the sign of the $^{55}$Mn hyperfine anisotropy has reversed relative to the RS and $I_3$ species, such that the unique axis $A_3$ now exhibits the smallest of the three values.

**Multifrequency EPR of R2lox Samples Prepared in $D_2O$ Shows Increased Anisotropy of the $I_4$ g- and A-Tensors.** In the RS of WT R2lox, a water ligand is coordinated to the $Mn^{III}$ directly, making up the unique g- and A-tensor axes, with a hydroxide bridging ligand to mediate electronic communication between the two metals. Protons on both of these ligands are susceptible to exchange for deuterons in solution, and a previous study of these systems used the exchanged deuterium signals to resolve the RS cofactor geometry.[20] To probe the protons in the ligand sphere of $I_4$, freeze-quenched samples were prepared using $D_2O$. While only slight changes were observed in the CW and pulsed field-swept spectra of the RS and $I_3$ species (Figure S6), the spectra of deuterated $I_4$ ($I_{4,D}$) appear broadened relative to the protiated data. While the most noticeable difference occurs at the high-field, $g_3$ turning point (Figure 4 and Figure S7), spectral simulations of $I_{4,D}$ within the projected basis required slight changes to the $g_1$ value as well as greater $^{55}$Mn hyperfine coupling constants and anisotropy (Table 1 and Figure S8). The increased spectral breadth seen for $I_{4,D}$ runs counter to typical observations of spectral narrowing in $D_2O$, which is generally attributed to the collapse of exchangeable proton hyperfine interactions; thus, a different mechanism must be responsible for the shift in spectral parameters. A better understanding of these changes was obtained through analysis of the spin Hamiltonian parameters within the intrinsic basis of each metal.

**Individual Site Parameters and Exchange Coupling Can be Extracted from Full Spin Hamiltonian Simulations.** Complete spin Hamiltonian simulations of $I_4$ that


https://doi.org/10.1021/jacs.1c13738
J. Am. Chem. Soc. 2022, 144, 11991−12006

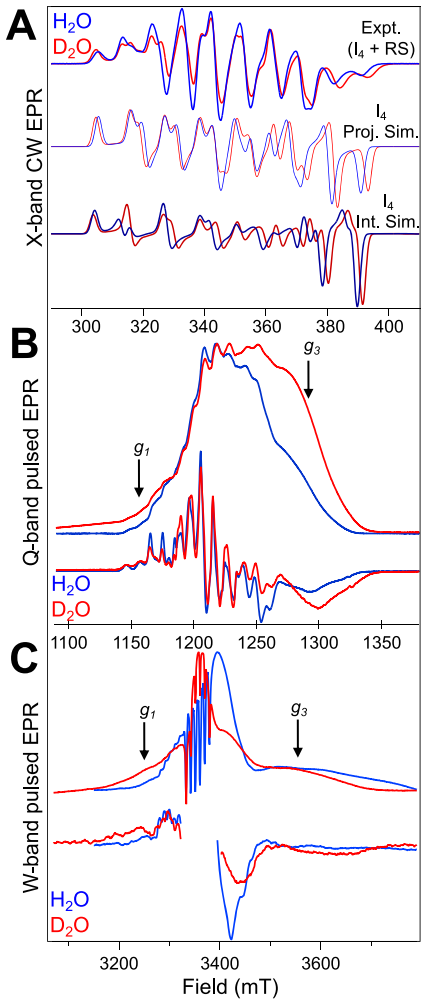


**Figure 4.** Multifrequency EPR spectra ($T$ = 5 K) of the WT $I_4$ species quenched at 45−60s in $H_2O$ (blue) and $D_2O$ (red). (A) X-band CW spectra ($P$ = 20 mW). (B) Pulsed Q-band ($t_\pi$ = 24 ns; $\tau$ = 200 ns) and (C) pulsed W-band ($t_\pi$ = 200 ns; $\tau$ = 850 ns) echo intensities and pseudo-modulated spectra with $g_1$ and $g_3$ indicated. As contributions from the RS are present in the experimental spectra, spin Hamiltonian simulations are shown for only the $I_4$ species in the projected basis (A, middle traces) and the intrinsic basis (A, bottom traces) using the parameters in Table 2.

considered the individual Fe and Mn ions, along with the exchange interaction between the metals, were employed to relate the projected parameters of the spin-coupled system to those in the intrinsic basis for each metal center. While all of the intrinsic spin Hamiltonian parameters cannot be uniquely fit from the multifrequency EPR spectra alone, the application of a few reasonable constraints and conditions reduces the size of the variable space to resolve key electronic parameters of $I_4$, including intrinsic g-values, zero-field splitting parameters (D, E/D), and the exchange coupling ($J$). The following approximations and assumptions were applied:

(1) Oxidation states: Given that the anisotropy of the $^{55}$Mn A-tensor is similar in magnitude to a $Mn^{III}$ rather than a $Mn^{IV}$ center, the metals were assigned to the $Mn^{III}/Fe^{III}$ (S = 2/S = 5/2) oxidation states.[44] This is also in line with the S = $^1/_2$ ground state of the system and persistent nature of the $I_4$ species—a higher-valence $Mn^{IV}/Fe^{IV}$ species would be expected to decay within seconds.[16]

(2) Exchange coupling: The large anisotropies of the projected g- and $^{57}$Fe A-tensors necessitate consideration of the electronic interaction between the metals within an intermediate regime, where $|J/D| < 10$.[45,46] Moreover, the relaxation of $I_4$ is more rapid than that of the RS (Figure S9), and temperature-dependent $T_1$ measurements are consistent with $|J| \leq 10$ cm$^{-1}$ for a dominantly Orbach relaxation mechanism (Figures S10 and S11; see methods for additional discussion).[20,39]

(3) Rhombicity: The pronounced rhombicity of the projected g-tensor suggests transfer of anisotropy from the intrinsic $Mn^{III}$ g-tensor, necessitating values that deviate non-negligibly from the free electron g-value.[45] The rhombicity of the $Mn^{III}$ ZFS was considered only in the limiting cases of fully axial (E/D = 0) and fully rhombic (E/D = 1/3) ZFS tensors (Figure S12).

(4) $Fe^{III}$ parameters: The $d^5$ $Fe^{III}$ state was assumed to have spherical symmetry, with $g_i$ = 2.0, $a_{aniso}$ = 0, and D = E/D = 0.

With these assumptions, values for D and $J$ were estimated using second-order perturbation theory for an intermediate-strength coupled system to fall between −1.5 and −3 cm$^{-1}$ and −3 and −6 cm$^{-1}$, respectively, given either an axial (E/D = 0) or fully rhombic ZFS tensor (E/D = 1/3). From this starting point, the spectra were simulated using the EasySpin toolbox,[47,48] resulting in the intrinsic spin Hamiltonian values shown in Table 2. A full description of the procedure followed is given in the Materials and Methods and the Supporting Information. Importantly, the spectral changes observed for $I_4$ prepared in $D_2O$ buffers, including the small changes in projected g- and $^{55}$Mn A-tensor values, can be reproduced within the full spin Hamiltonian simulation by varying only the exchange coupling, which decreases in magnitude from −2.4 to −2.33 cm$^{-1}$. A direct comparison to the multifrequency experimental spectra constrained the parameters further (Figure S13), though within the resolution of the experimental data, the rhombicity of the $Mn^{III}$ ZFS cannot be fully resolved and thus was constrained to be axial to reduce the number of variables (Figure S14). At W-band frequencies, the Zeeman term is of the same order of magnitude as the exchange coupling and the zero-field splitting, which has been shown to result in complex lineshapes (Figures S13 and S14).[49] This may indeed be manifested in the experimental spectra, as the features of $I_4$ are less well-resolved at the W-band. However, the excellent agreement between the projected and intrinsic spectral features, including the g- and $^{57}$Fe hyperfine tensors, at both X- and Q-bands, supports the simulated on-site parameters for $Mn^{III}$. Moreover, these simulations quantify the effect of the isotopic substitution on the exchange interaction between the metals, the origin of which is discussed below.

**Pulsed Hyperfine EPR Techniques Examine Interactions between Mn/Fe Active Site and Ligand Nuclei with High Resolution.** Beyond the selective characterization of individual species within a reactive mixture, pulsed EPR techniques offer the opportunity to resolve interactions between a spin system and weakly coupled nuclei, revealing parameters such as metal−ligand distances, orientation, and even ligand protonation state. The spectral breadth of $I_4$ can be leveraged to obtain single-crystal-like hyperfine spectra at the low-field and high-field turning points, selecting for that intermediate within the freeze-quenched mixture of species.


https://doi.org/10.1021/jacs.1c13738
J. Am. Chem. Soc. 2022, 144, 11991−12006

**Table 2. Simulated and Calculated Intrinsic Spin Hamiltonian Parameters for the RS and Intermediate Species**

| | | | $Mn^{III}$[b] | | intrinsic $a_i$ | | |
|---|---|---|---|---|---|---|---|
| | | J/ $cm^{-1}$[a] | D/ $cm^{-1}$ | E/D /$cm^{-1}$ | | $Mn^{III}$ | $Fe^{III}$ |
| $I_3$ | expt.[c] | −40 | | | \|1\| | 209 | 28.2 |
| | | | | | \|2\| | 272 | 27.9 |
| | | | | | \|3\| | 181 | 23.1 |
| | | | | | $\|a_{iso}\|$ | 221 | 26.4 |
| | | | | | $\|a_{aniso}\|$ | 77 | −5.0 |
| | calc | −151 | −2.3[b] | 0.28 | $x$ | 69 | −11 |
| | | | | | $y$ | 158 | −18 |
| | | | | | $z$ | 241 | −37 |
| | | | | | $a_{iso}$ | 156 | −22 |
| | | | | | $a_{aniso}$ | 131 | 23 |
| $I_4$ | expt. $H_2O$[d] | −2.40 | −1.60 | 0 | \|1\| | 210 | |
| | | | | | \|2\| | 480 | 30 |
| | | | | | \|3\| | 150 | |
| | | | | | $\|a_{iso}\|$ | 280 | 30 |
| | expt. $D_2O$ | −2.33 | | | $\|a_{aniso}\|$ | 300 | 0 |
| | calc.[e] | −22.0 | −1.64 | 0.02 | $x$ | −156 | 20 |
| | | | | | $y$ | −157 | 21 |
| | | | | | $z$ | −294 | 22 |
| | | | | | $a_{iso}$ | −202 | 21 |
| | | | | | $a_{aniso}$ | −138 | 1.5 |
| RS | expt. | −5 | −3.20 | | 1 | 270 | 32.0 |
| | | | | | 2 | 260 | 26.4 |
| | | | | | 3 | 127 | 29.2 |
| | | | | | $a_{iso}$ | 219 | 29.2 |
| | | | | | $a_{aniso}$ | −138 | 4.2 |
| | calc. | −20.6 | −1.57 | 0.29 | $x$ | −66 | 26 |
| | | | | | $y$ | −148 | 21 |
| | | | | | $z$ | −237 | 22 |
| | | | | | $a_{iso}$ | −150 | 23 |
| | | | | | $a_{aniso}$ | −130 | 4.5 |

[a]All of the $J$ values are reported in the $H = -2JS_1S_2$ convention. [b]D and E/D for $Mn^{III}$ are calculated using a $Ga^{III}$-substituted structure in place of $Fe^{III}$. [c]Intrinsic experimental $a$ values for $I_3$ were calculated by applying isotropic spin projection factors of −4/3 and 7/3 to the $Mn^{III}$ and $Fe^{III}$-simulated projected hyperfine values. [d]Simulations of $I_4$ used intrinsic g values of [1.984 1.875 1.973] for $Mn^{III}$. [e]Calculations of $I_4$ were performed using the optimized protiated structure.

Deep modulations in the 3-pulse ESEEM traces at Q-band reveal strong coupling between the $I_4$ active site and a nitrogen atom, as evidenced by the presence of peaks consistent with near-exact cancellation conditions for an I = 1 nucleus (Figure 5).[50,51] Simulations of this nucleus across both field positions within the projected basis reveal a rhombic hyperfine tensor with $|A(^{14}N)|_{iso}$ = 11 MHz, $A_{dip}$ = 2.1 MHz, and $\eta$ = 0.85, with Euler angles $[\alpha, \beta, \gamma] = [92°, 52°, 120°]$ to rotate the A-tensor with respect to the projected g-tensor. The quadrupole contribution was simulated with $e^2qQ/h$ = 2.9 MHz and $\eta$ = 0.6, with the quadrupolar frame rotated from the g-tensor by $[\alpha, \beta, \gamma] = [32°, 43°, 12°]$ (Figure S15). This signal likely corresponds to histidine-105, which is bound to the $Mn^{III}$ center, as discussed further below.

Signals from more weakly coupled $^{14}N$ nuclei become apparent in the HYSCORE spectra of $I_4$, also measured at the low- and high-field turning points (Figure 5C,D and Figure S16). Preliminary simulations suggest that these features can be approximately reproduced with a hyperfine tensor of $|A(^{14}N)|_{iso}$ = 2.5 MHz, $A_{dip}$ = 1.3 MHz, and $\eta$ = 0.3, and a quadrupole contribution of $e^2qQ/h$ = 1.4 MHz and $\eta$ = 1; however, because the signals are masked in the Q-band ESEEM traces due to the deep modulations of the dominant $^{14}N$ species, complete resolution of the hyperfine tensor will require X-band ESEEM or complementary techniques.[20,52,53]

The protonation states of ligands bound to $I_4$ were probed using Q-band ESEEM and HYSCORE as well as W-band electron−electron double-resonance detected nuclear magnetic resonance (ELDOR-detected NMR; EDNMR) techniques applied to samples prepared in both protiated and deuterated buffers (Figure 6). As with the $^{14}N$ characterization, the low- and high-field g-tensor turning points were selected to provide orientation selection. In the $I_{4,D}$ samples, deep modulations of the ESEEM traces due to the presence of deuterium nuclei were observed at both field positions, with a strong dependence on the interpulse spacing, $\tau$ (Figure 6A and Figures S17 and S18). These features are pronounced in the Fourier-transformed ESEEM traces and are better separated from the $^{14}N$ bands in the Q-band HYSCORE spectra, which, at low field, reveal a pronounced ridge with two features separated by approximately 2.5 MHz (Figure 6B). At high field, the off-diagonal peaks appear cylindrical and split by only 1.6 MHz, consistent with strong, highly anisotropic coupling to a $^2H$ nucleus (Figure 6D and Figures S19 and S20).[20,37] Further orientation and species selection was obtained through the use of W-band EDNMR spectra,[54−57] which were collected on $I_4$ and $I_{4,D}$ as well as on samples of WT R2lox reconstituted with $Mn^{II}$-only (Figure 6C,E). At $g_1$, two sets of features are observed in the $H_2O$ sample, split around the $^1H$ Larmor by ∼12 MHz and ∼6 MHz. These signals are not present in the $Mn^{II}$-only control and are well-resolved upon subtraction of the $Mn^{II}$ R2lox data from $I_4$ (Figure S21). Spectra of $I_{4,D}$ measured at $g_1$ show a feature centered approximately 2 MHz around the $^2H$ Larmor that is absent in $Mn^{II}$ R2lox, which is also better resolved by subtraction of the datasets (Figure 6D and Figure S21). The EDNMR spectra of $I_4$ and $I_{4,D}$ collected on the high field $g_3$ turning point also show a small H signal (Figure 6E). The EDNMR spectrum of $I_{4,D}$ collected at $g_3$ is significantly narrower than the corresponding control data, which reflects the selectivity of the technique and indicates that only a minor population of $Mn^{II}$ R2lox is probed within the $I_{4,D}$ sample. The rapid relaxation of the $I_4$ species and limited spectral bandwidth precluded measurement of more weakly coupled $^1H$ signals through ENDOR or Q-band HYSCORE spectroscopy.

**Broken-Symmetry Density Functional Theory Calculations Provide Structural Models of $I_3$ and $I_4$.** In recent years, broken-symmetry density functional theory (BS-DFT) calculations have been of great utility in the study of exchange-coupled, multinuclear transition metal compounds, with


https://doi.org/10.1021/jacs.1c13738
J. Am. Chem. Soc. 2022, 144, 11991−12006

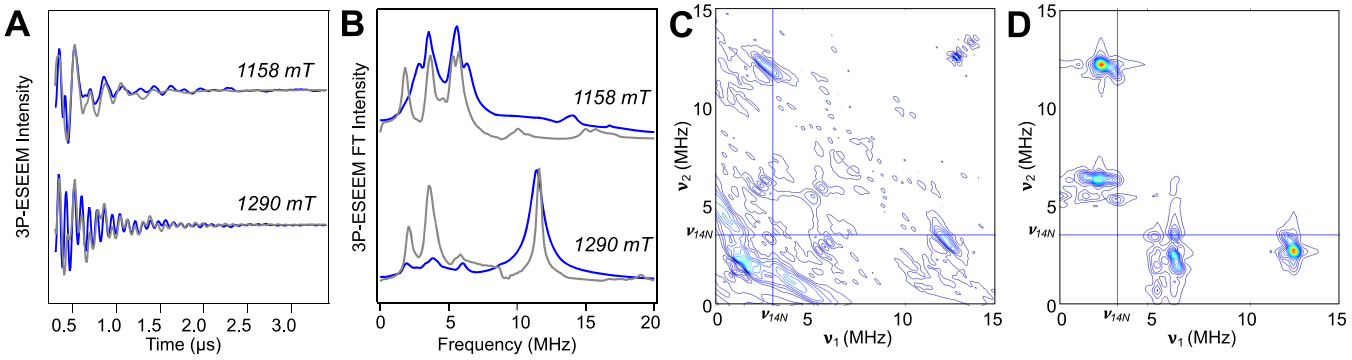


**Figure 5.** $^{14}$N Q-band hyperfine spectra of $I_4$. (A) Three-pulse ESEEM time domain and (B) Fourier transform spectra of $I_4$ prepared in $H_2O$ buffer measured at the $g_1$ and $g_3$ turning points (as indicated). (C) Experimental HYSCORE spectrum at the $g_1$ turning point. (D) Simulated HYSCORE at the $g_1$ turning point. Simulations are generated from the following parameters: $[A_1, A_2, A_3]$ = [7, 10.5, 15] MHz, $[\alpha, \beta, \gamma]$ = [92°, 52°, 120°], $[Q_1, Q_2, Q_3]$ = [2.3, −2.9, 0.5] MHz with $[\alpha, \beta, \gamma]_Q$ = [32°, 43°, 12°]. Experimental parameters: $T$ = 5 K; $t_\pi$ = 24 ns; $\tau$ = 200 ns; $T$ = 100 ns; $dx$ = 8 ns (ESEEM), $dx/dy$ = 16 ns (HYSCORE); points = 512 (ESEEM), 256 (HYSCORE).

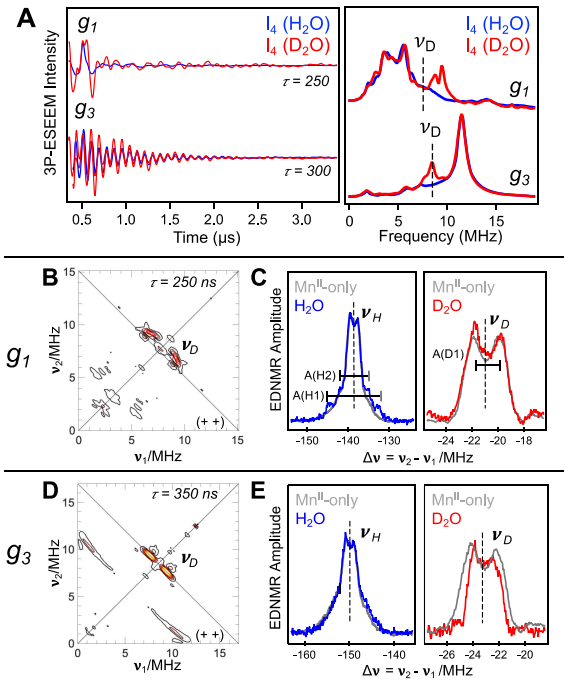


**Figure 6.** Orientation-selective hyperfine characterization of exchangeable protons in $I_4$. Pulsed EPR data were collected on $I_4$ samples at either the $g_1$ or $g_3$ turning points (as indicated); nuclear Larmor frequency ($\nu$) indicated with dashed lines. (A) Q-band 3-pulse ESEEM collected on samples prepared in $H_2O$ (blue) or $D_2O$ (red). Baseline-corrected time domain data are shown after subtraction of the exponential echo decay (left) with the corresponding Fourier-transform (right). Experimental parameters: ($T$ = 5 K; $t_\pi$ = 24 ns; $\tau$ = 250 ns ($g_1$, 1158 mT) or 300 ns ($g_3$, 1290 mT); $T$ = 100 ns; $dx$ = 8 ns; points = 512). (B,D) Q-band HYSCORE of $I_{4,D}$ showing the weak-coupling (+,+) quadrant, with the diagonal and anti-diagonal intersecting at $\nu_D$. Experimental parameters: ($T$ = 5 K; $t_\pi$ = 16 ns; $\tau$ = 250 ns ($g_1$, 1158 mT) or 350 ns ($g_3$, 1290 mT); $T_1/T_2$ = 200 ns; $dx$ = $dy$ = 16 ns; points = 256). (C,E) W-band EDNMR spectra collected on $I_4$ prepared in $H_2O$ (blue) or $D_2O$ (red) and R2lox reconstituted with only $Mn^{II}$ in $H_2O$ or $D_2O$ (gray). Experimental parameters: ($T$ = 5 K; $t_\pi$ = 200 ns; $\tau$ = 1500 ns; $T$ = 500 ns; HTA = 7.5 $\mu$s; $B_0$ = 3200 mT ($g_1$), 3560 mT ($g_3$)).

particular application for understanding the electronic structure of the water oxidizing complex (WOC) of photosystem II (PSII) and related models.[58−61] To complement the pulsed EPR studies, BS-DFT studies on possible $I_3$ and $I_4$ structures were performed. An active site cluster model was constructed that included the outer-sphere residue Y175, previously shown to impact the resting state electronic structure through modulating the hydrogen-bonding network around the active site (Figure 7).[11] In addition, it was necessary to include the outer-sphere D201 residue for geometry optimizations of $I_3$. This residue, which immediately precedes the "switching carboxylate" of the second metal site, is conserved across most members of the ferritin-like superfamily and provides a hydrogen bond to the histidine residue of the first metal-binding site.[62−64] Attempts to optimize any intermediate structures without this residue led to loss of coordination of the histidine residue and substantial distortion of the optimized structure, which was considered physically unreasonable (Figure S22). Benchmark calculations performed on the RS structure, including the fatty acid ligand, gave structures and calculated values for the exchange coupling and intrinsic hyperfine tensors that were in good agreement with previously published values. While the magnitude of the exchange coupling is overestimated relative to the experimentally resolved values, the signs of $J$ and relative trends between RS, $I_3$, and $I_4$ were reproduced, and similar methodology was adopted for the study of intermediates $I_3$ and $I_4$. (Table 2 and Figure 7).[20] Model geometries for the $I_3$ and $I_4$ species were constructed that included both 5- and 6-coordinate metal centers, bridging oxo and hydroxo ligands, and terminal hydroxo and aquo ligands (Figures S23−S25). For each model, the structure was optimized within the BS formalism prior to calculating the hyperfine tensors for $^{55}$Mn and $^{57}$Fe as well as the exchange coupling energetics (Table S1). Substitution of $Fe^{III}$ with $Ga^{III}$ was used to calculate the intrinsic and zero-field splitting parameters of the $Mn^{III}$ ion (Table 2).[65,66] Spectral simulations in the intrinsic basis using the DFT-calculated values were compared to experimental data for each of the optimized models (Figures S26 and S27). The energies of each species across protonation states were also evaluated (Table S2). Antiferromagnetic coupling was predicted for most model structures, consistent with the experimentally observed $S = {}^1/_2$ ground state; models for which ferromagnetic coupling was calculated were not considered further. The structures of all models have reasonable geometric parameters (Table S3). Natural orbital localization of the optimized $I_3$ models reveals a rotated, Mn-


https://doi.org/10.1021/jacs.1c13738
J. Am. Chem. Soc. 2022, 144, 11991−12006

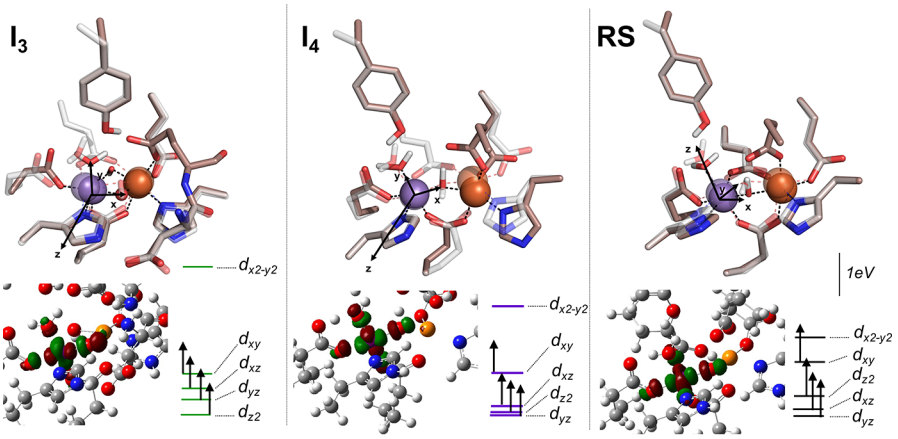


**Figure 7.** DFT structural models, LUMO contour plots, and MO diagrams of $I_3$, $I_4$, and RS. (Top) Optimized structures (beige) overlaid on the RS crystal structure (gray, PDB 4HR0). All hydrogen atoms except those involved in the hydrogen bonding network have been omitted for clarity. Principal axes labeled on $Mn^{III}$. (Bottom) LUMO of each structure and semi-quantitative frontier MO diagram for Mn-localized natural orbitals. Relative MO energies are given according to the scale bar on the right-hand side.

centered LUMO that resembles the $d_{x2-y2}$ orbital, similar to the R2c-like species reported previously, with an elongated unique axis that is rotated relative to the unique axis in the RS (Figure 7). Similar LUMOs are calculated for the $I_4$ models.[67,68] The d-orbital splitting reorders between the two models, with the low-lying $d_z^2$ orbital in the $I_3$ models reflecting the long bonds to the His105 and $\mu$-OH ligands along the $Mn^{III}$ $z$ axis. These frontier molecular orbitals are consistent with $D < 0$, as revealed from the full SH simulations of $I_4$ (*vide supra*),[69−71] and the calculated values of the $Mn^{III}$ ZFS obtained from $Ga^{III}$-substituted structures. The BS-DFT exchange coupling is overestimated relative to the experimental values for all models of $I_3$ and $I_4$, though to a similar extent as observed in the computational model of the RS. As expected, the calculated $J$ values increase when the metals are bridged by an oxo ligand, rather than a hydroxo ligand.[20,59,72] An isotropic hyperfine tensor was predicted for the $^{57}$Fe center in almost all $I_4$ models, consistent with a spherically symmetric $d^5$ configuration.[45] Notably, the magnitude of $^{55}$Mn coupling, while remaining near-axial in all cases, was significantly underestimated in the 6-coordinate models of $I_4$, likely due to increased transfer of spin onto the Fe center. Considering all of the calculated parameters, the favored model for $I_3$ features a $Mn^{III}(\mu$-$O)(\mu$-$OH)Fe^{III}$ active site with a terminal aquo ligand (Model 7, Figure S25). This model was selected on the basis of agreement with the observed spectral parameters and energetics; models that included a terminal hydroxide ligand to $Mn^{III}$ were calculated to lie substantially higher in energy than those with a terminal aquo ligand. While we present the model for which the bridging hydroxo lies on the face that the fatty acid occupies in the RS, the calculated spectral and energetic properties are not sufficiently distinct for us to resolve the site of protonation, and the isomer in which the other bridging ligand is protonated cannot be excluded. The favored structure for $I_4$ features 5-coordinate $Mn^{III}$ and $Fe^{III}$ centers, with a single bridging hydroxide ligand and a terminal aquo ligand (Model 2, Figure S23). This model shows the best agreement with the experimental parameters for $I_4$ as derived from the full spin Hamiltonian simulations and lies significantly lower in energy than the corresponding model with a terminal hydroxide species (Figure 7).

## DISCUSSION

**The $I_3$ R2lox Intermediate Represents an R2c-like Cofactor.** The spectral and relaxation properties of $I_3$ are similar to those reported for the dithionite-reduced R2c protein[6,7] as well as a species observed in a glycine-to-leucine mutant (G68L) of R2lox (Table 1),[37] providing strong evidence that this signal derives from a $Mn^{III}(\mu$-$O)(\mu$-$OH)Fe^{III}$ species. Further evidence in support of this assignment comes from recent characterization of a small-molecule model of R2lox reported by Que and coworkers, which features $(\mu$-$O)(\mu$-$OH)$ bridging ligands between $Mn^{III}$ and $Fe^{III}$ and has nearly identical projected SH parameters to those simulated for $I_3$.[73] The relaxation properties indicate a much greater exchange coupling between the metals than in the RS species, consistent with the presence of at least one oxo bridge and in line with the geometric and electronic structures suggested by the DFT calculations (Table 2). The asymmetry of the protein environment likely compels protonation of one of the putative $O_2$-derived bridges to be preferentially favored over another; however, we are unable to resolve which bridge features the protonated ligand on the basis of our current calculations or spectroscopic data. We hypothesize this may be relevant for further turnover processes and suggest that differences in the protonation site or hydrogen bonding network may contribute to the larger exchange coupling observed for $I_3$ than was reported for the G68L mutant.[37] Ongoing work is aimed at resolving the protonation site through selective labeling and complementary studies of mutants. The $I_3$ state represents an intermediate along the proposed WT Mn/Fe oxidative assembly pathway,[32] occurring concomitantly with carbocation formation upon reduction of the transient $Mn^{IV}/Fe^{III}$ state. This process thus reflects a point of overlap between the one-electron-oxidizing R2c proteins and the two-electron-oxidizing R2lox proteins, with the $Mn^{IV}/Fe^{III}$ and $Mn^{III}(\mu$-$O)(\mu$-$OH)Fe^{III}$ species serving as shared states across the divergent enzyme classes.[14,32,74,75]

**The $I_4$ Intermediate Is Unique to the R2lox Proteins.** While spectral signals similar to $I_3$ have now been observed across two different protein and model systems, the EPR spectrum of $I_4$ is quite unusual. The spectral breadth and g-tensor anisotropy exceed that of any previously characterized Mn/Fe species, reflecting the weak hydroxide-mediated


https://doi.org/10.1021/jacs.1c13738
J. Am. Chem. Soc. 2022, 144, 11991−12006

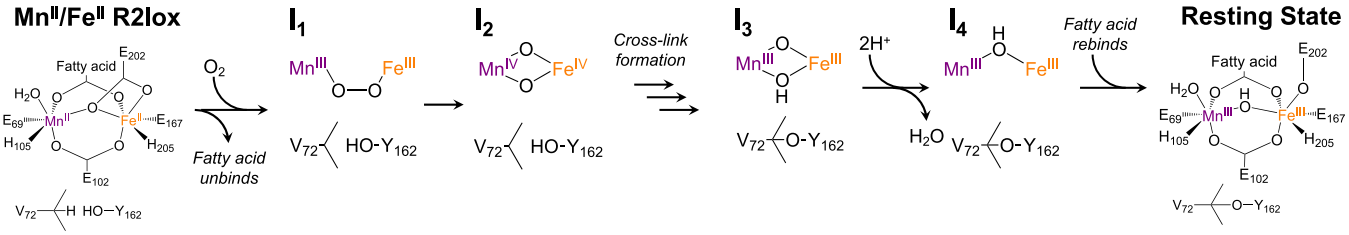


**Figure 8.** Proposed aerobic assembly mechanism of Mn/Fe R2lox.

exchange coupling between the trivalent metals. The EPR signatures of a bridging hydroxide ligand in mixed-valence diiron proteins have been resolved previously through ENDOR and HYSCORE studies, showing broad and anisotropic signals of up to 20 MHz.[25,26,28,76,77] The spectral features of the exchangeable proton in $I_4$ closely resemble those previously reported in proteins such as methane monooxygenase and uteroferrin,[25,26,76] including the ∼12 MHz $^1$H coupling seen in the W-band EDNMR spectra and the deep $^2$H modulations in the Q-band HYSCORE spectra, further supporting the assignment of a single $\mu$-OH bridge.

The shifts in the projected g-tensor upon isotopic H/D substitution highlight the potential for EPR of spin-coupled systems to report on subtle shifts in hydrogen-bonding networks, as these readily apparent changes can be reproduced by including a 3% decrease in the simulated intrinsic $J$ values of $I_4$. The isotope-induced spectral changes were correlated to structural changes through single-point calculations. The O−H bond distance was scanned around the optimized $I_4$ geometry, and the exchange coupling was calculated for each position (Figure S28). To access an analogous 3% change in the calculated $J$ values (i.e., a decrease from −22.0 to −21.3 cm$^{-1}$) would imply a decrease in the O−D bond length of approximately 4% relative to the optimized structure. The hydrogen bonding distance to the E202 carboxylate would thus be expected to increase by 2.5%. These changes are similar to the isotope-dependent structures previously reported for liquid water, where the O−H bond distance was modeled to decrease by 3% in $D_2O$ and intermolecular hydrogen bonds were found to be 4% longer.[78] Importantly, this distance resolution, as reflected here by small changes in SH parameters upon isotopic exchange, is unattainable by any crystallographic or X-ray spectroscopic technique and may find further application in resolving protonation states and exchange coupling parameters in other multinuclear systems. For example, the EPR spectrum of the Mn$^{III}$/Fe$^{III}$ resting state of the Y175F R2lox mutant exhibits slightly narrowed spectral breadth relative to WT R2lox, consistent with a change in exchange coupling that derives from differences in the hydrogen bonding network around the active site.[11] Interestingly, the $I_4$ intermediate in Y175F shows substantially greater spectral breadth (Figure S29) as well similar sensitivity to isotopic substitution as WT R2lox. While a full analysis of the Y175F intermediate structure is beyond the scope of this manuscript, the similarity in spectral properties suggests a similar structure, with the slight differences in hydrogen bonding leading to dramatic changes in the projected EPR spectrum. Other biological examples where resolving these changes in EPR spectra could translate into understanding perturbations to hydrogen bonding networks include the spin-coupled systems of Mn catalase,[79,80] photosystem II,[53,81,82] and iron−sulfur clusters.[83,84] Importantly, in WT R2lox, no isotope effects are seen in the spectra of $I_3$ (Figure S6), which is attributed to the strong oxo bridging ligand. As such, isotope-dependent spectra can be considered a hallmark of systems that fall in the weak-to-intermediate exchange-coupling regime. A comparison between the exchange coupling and ZFS parameters of R2lox and other systems that fall into this regime is given in Table S4.

The $^{14}$N hyperfine interactions support the DFT-optimized structure of $I_4$. The isotropic $^{14}$N coupling is much greater than seen for the R2lox RS species or histidine ligands bound to Mn catalase[52] or photosystem II[53,85,86] and more closely resembles the hyperfine coupling seen for Mn$^{III}$ porphyrin species with bound nitrogenous axial ligands.[52] In these cases, the $z$ axis lies along the Mn−N bond, such that the singly occupied $d_{z^2}$ orbital gives rise to large coupling. The rotation of the unique $z$ axis to lie along the Mn−N vector is consistent with the absence of the fatty acid ligand, which would lie along this axis, as the energy of the $d_{z^2}$ would decrease upon loss of this coordinating ligand. The lower energy of the $d_{z^2}$ orbital in $I_4$ relative to the RS is manifested in the DFT calculations (Figure 7), further supporting the validity of the computational model.

**The $I_4$ State Is Primed for Substrate Addition.** Based on the pulsed EPR data in conjunction with the BS-DFT calculations, we propose an aerobic assembly mechanism for the R2lox cofactor that integrates the structural information obtained in this study with previous suggestions (Figure 8). The two early species formed upon $O_2$ addition, with optical features at 620 and 390 nm, accumulate to a sufficiently low degree that they are not observed in EPR, particularly when considering the background signals from Mn$^{II}$, the $I_3$ and $I_4$ species, and the RS. The $I_3$ species is formed after O−O bond cleavage and represents a branching point between R2lox and R2c chemistry. That the common species in the only two redox-active Mn/Fe proteins characterized to date features a Mn$^{III}$($\mu$-O)($\mu$-OH)Fe$^{III}$ core rather than the conventional Fe$^{III}$($\mu$-O)$_2$Fe$^{III}$ state seen across most diiron carboxylate proteins[1,71] likely derives from the lower Lewis acidity of a Mn$^{III}$ ion relative to an Fe$^{III}$ ion and may be generalizable across different classes of Mn/Fe proteins and cofactors. This distinction is expected to map onto reactivity, lowering the propensity of the Mn/Fe cofactor toward hydroxylation and promoting alternative reactions following C−H bond activation.[9,18]

Protonation of $I_3$ to release $H_2O$ generates $I_4$, which has an open coordination site on each metal. Characterization of this long-lived, coordinatively unsaturated species has implications for understanding subsequent reactivity. The principal axis lies along the open site, with an electron in the $d_{z^2}$ orbital available for interaction with an incoming substrate. While direct substrate coordination to the active site is not standard in the diiron carboxylate proteins, it has been observed in some members, including the recently characterized fatty acid


https://doi.org/10.1021/jacs.1c13738
J. Am. Chem. Soc. 2022, 144, 11991−12006

decarboxylase UndA.[87,88] We thus propose that $I_4$ is the catalytically competent state, poised for substrate and/or $O_2$ binding. As the spectral signatures of the $I_4$ species are highly sensitive to the local environment, including changes in hydrogen bonding networks, we suggest that the EPR spectra of $I_4$ can be used to reveal downstream R2lox function.

## CONCLUSIONS

The electronic and geometric structures of two cofactor assembly intermediates in the heterobimetallic Mn/Fe protein R2lox have been characterized using multifrequency pulsed EPR spectroscopy in conjunction with full spin Hamiltonian simulations and broken symmetry density functional theory calculations. The $I_3$ intermediate is suggested to have both a bridging oxo and a bridging hydroxo ligand, giving rise to large exchange coupling between the trivalent metals. This type of species is found in both classes of Mn/Fe proteins and is suggested to represent a branching point between the R2c and R2lox proteins, where the metals in the former enzyme must remain coordinatively saturated to support rapid electron shuttling. Ongoing work is aimed at understanding why this species is stable in R2c yet transient in R2lox and may reveal molecular factors within the protein scaffold and active site environment that govern one- vs two-electron reactivity. The $I_4$ species is unique among the R2lox proteins, with weak antiferromagnetic exchange coupling between the two metals that reflects a single, bridging hydroxide ligand engaged in strong hydrogen bonding. The similarity in magnitude between the exchange coupling and the local zero-field splitting on $Mn^{III}$ renders EPR spectroscopy particularly useful to probe small geometric changes, including those induced upon isotopic substitution. Here, we illustrate how those changes report on the H-bonding network and outer coordination sphere changes around the cofactor. Ongoing work is focused on correlating the electronic structure parameters of the $I_4$ intermediate, implicated as the species that immediately precedes substrate binding, with reactivity. Ultimately, the EPR methodology presented here can be generally applied across diverse protein systems and may aid in the identification of additional classes of Mn/Fe proteins.

## MATERIALS AND METHODS

**EPR Sample Preparation.** The R2lox protein (either the WT or the Y175F variant) from *Geobacillus kaustophilus* (*Gk*R2loxI) was expressed heterologously in *E. coli* and purified in its apo form as previously described.[9,11,32] To reconstitute the Mn/Fe cofactor, solutions of apo-R2lox were first prepared via dilution of concentrated protein stocks into $O_2$-saturated buffer E (100 mM HEPES, 50 mM NaCl, pH = 7.0). For $D_2O$ samples, apo-R2lox was first buffer exchanged into buffer F (buffer E prepared using $D_2O$; Sigma-Aldrich) and allowed to incubate 12−16 h prior to dilution into $O_2$-saturated buffer F. Metal stocks of either $MnCl_2{\cdot}4H_2O$ (Amresco) or $(NH_4)_2Fe(SO_4)_2{\cdot}6H_2O$ (Sigma-Aldrich) were made by dissolving each in deionized water to a concentration of 0.1 M; $^{57}Fe$ samples were prepared using frozen stocks of 10 mM $^{57}Fe^{II}$ as described previously.[32] These metal stocks were then diluted into an $O_2$-saturated, 40% v/v aqueous glycerol solution made using either deionized water or $D_2O$.

Solutions of apo-R2lox and metals were hand-mixed in a 1:1 ratio, giving final concentrations of ∼800 μM (WT) or ∼530 μM (Y175F) and 20% glycerol. Metals were kept at an equal concentration to each other but substoichiometric to apo-R2lox, with either 0.5 (WT) or 0.75 (Y175F) equivalents each of $Mn^{II}$ and $Fe^{II}$ used. The same protocol was followed to generate $Mn^{II}$-only samples, with 0.5−1 equivalents of $Mn^{II}$ mixed with apo-R2lox and allowed to incubate for several hours prior to freezing in liquid nitrogen. Samples used to generate the relative concentration profiles shown in the inset of Figure 2 were generated from a combination of rapid-freeze-quenched samples ($t \leq 60$ s) and hand-quenched samples ($t \geq 60$s) as described in ref 32.[32] Kinetic modeling using the mechanism and rate constants presented in ref 11 was carried out using the Kintek software package[89] to compare the relative expected appearance of $I_3$ and $I_4$ (Figure S30).

To generate EPR samples of $I_3/I_4$, ∼150 μL (X-band), ∼30 μL (Q-band), or ∼ 90 μL (W-band) of the reacting solution were loaded into sample holders. Reactions were quenched at 35−60s via freezing in an isopentane-liquid nitrogen bath held below 170 K. Sample holders for the X-band (735-PQ-250M) and Q-band (WG-222T-RB) were quartz EPR tubes purchased from Wilmad Lab-Glass. Sample holders for W-band measurements were custom-built, cylindrical Rexolite sample holders machined in-house at the National High Magnetic Field Laboratory (NHMFL).[90]

**Multifrequency EPR Data Collection.** X-band CW EPR spectra were collected at 5 K in the Ohio Advanced EPR Facility at Miami University (Oxford, OH) using a Bruker EMX instrument equipped with an Oxford Instruments continuous flow helium cryostat and temperature controller (ESR 900). The spectra of the $^{57}Fe$ and $^{2}H$ labeled WT $I_4$ species were collected at 5 K in the Analytical Spectroscopy Lab at Ohio State University using a Bruker EMXPlus instrument equipped with a ColdEdge cryogen-free helium recirculation system and an Oxford Instruments MercuryITC. All spectra were obtained using a microwave power of 20 mW, with a modulation frequency and amplitude of 100 kHz and 10 G, respectively, unless otherwise stated.

Q-band pulsed EPR spectra were collected at 5 K in the Ohio Advanced EPR Facility at Miami University (Oxford, OH) using a Bruker ELEXSYS 580 instrument equipped with a 300 W TWT amplifier, an ER 5107D2 pulsed Q-band resonator, and an Oxford Instruments continuous flow helium cryostat and temperature controller (ESR 900). W-band pulsed EPR spectra were collected at 5 K at the NHMFL (Tallahassee, FL) on a custom-built, high power (∼1 kW) quasi-optical 94 GHz EPR spectrometer (HiPER).[57]

Q- and W-band electron spin echo-detected (ESE) field swept spectra were measured using the pulse sequence $t_p-\tau-2t_p-\tau-$echo. The length of the $\pi/2$ microwave pulse was set to $t_p = 12$ (Q-band) or 100 ns (W-band). The interpulse distance was $\tau = 200$ (Q-band) or 850 ns (W-band). At Q-band the shot repetition time (SRT) was 100 μs, at W-band the sequence repetition frequency was 5 kHz. Q-band $T_1$ inversion recovery experiments were collected using the pulse sequence $2t_p-T-t_p-\tau-2t_p-\tau-$echo, where $T$ was set as 800 ns for the initial scan and then incremented ($dx = 16$ ns) in each subsequent measurement, for a total of 2048 measurements. The echo intensities for each measurement are then plotted vs time to give the inversion recovery traces.

Q-band 3-pulse ESEEM spectra were collected using the pulse sequence $t_p-\tau-t_p-T-t_p-\tau-$echo, with $t_p = 12$ ns and $T = 100$ ns, the interpulse distance was sampled in the range $\tau = 200-400$ ns. The timebase increment ($dx$) was 8 ns with 512 points collected. Q-band HYSCORE spectra were measured using the pulse sequence $t_p-\tau-t_p-T_1-2t_p-T_2-t_p-\tau-$echo. A pulse length of $t_p = 12$ ns was used, with the interpulse distances $T_1/T_2$ set to 200 ns; the interpulse distance was sampled in the range $\tau = 200-400$ ns. The timebase increments ($dx/dy$) were both set to 16 ns and 256 points collected. The SRT was set to 100 μs in both experiments.

W-band EDNMR was collected using the pulse sequence $t_{HTA}-T-t_p-\tau-2t_p-\tau-$echo, using a high turning angle (HTA) pulse of length $t_{HTA} = 7.5$ μs, a pulse length of $t_p = 100$ ns, an interpulse distance of $\tau = 1500$ ns, and a $T = 500$ ns. The sequence repetition frequency was set to 5 kHz. The microwave frequency of $t_{HTA}$ was swept in 0.1−0.2 MHz steps; the microwave frequency of the detection sequence was held at 94 GHz.

**Variable-Temperature EPR Relaxation Experiments.** Temperature-dependent relaxation properties of $I_3$ were obtained through power saturation measurements from 10−40 K using microwave powers from 2 μW−80 mW. The intensity of features from $I_3$ at the


https://doi.org/10.1021/jacs.1c13738
J. Am. Chem. Soc. 2022, 144, 11991−12006

low-field position (300 mT) was plotted as a function of power to find the $P_{1/2}$ value using eq 1:[39]

$$S(\text{signal}) = C\sqrt{P}/\sqrt{1 + P/P_{1/2}} \quad (1)$$

To estimate the energy spacing ($\Delta$) between the ground state and the first excited state assuming an Orbach relaxation process, the slope of $\ln(P_{1/2})$ plotted against inverse temperature was obtained (Figure S2). The exchange coupling $J$ was calculated as $\Delta/3$.[20] The Curie behavior of the signal intensity on 1/T was non-linear due to saturation effects (Figure S1).

The temperature-dependent relaxation properties of $I_4$ were probed using variable temperature EPR experiments at X- and Q-bands. Q-band $T_1$ relaxation measurements at 1157 mT ($g_1$) and 1290 mT ($g_3$) were collected from 4.8−10 K (Figures S10 and S11). Fitting the inversion recovery data to an exponential function provides the $\tau$ value, or recovery time constant, as the $T_1$ relaxation time.[91,92] To model the Orbach relaxation process, which assumes relaxation is dominated by the presence of low-lying excited states, the natural log of $1/\tau$ is plotted against the inverse of the collection temperature, and linear fits to the data provide the slope, $\Delta$. When the Orbach process dominates, this slope is an estimation of the energetic separation between the ground and first excited states and the exchange interaction may be determined from this estimate using the relationship $\Delta = 3J$.[93]

In the inversion recovery data collected on $I_4$, both a fast and slow relaxing component were present, necessitating the use of double exponential fits. As $Mn^{II}$ is ever present in these freeze-quenched assembly intermediates and likely contributes to the slowly relaxing component of the signal, only the time constant of the faster component ($\tau_1$) was selected (Figure S11A). Linear fits to the data were obtained from 4.8−5.9 K (see below) at $g_1$ (Figure S11B) and 4.8−7.7 K at $g_3$ (Figure S11C). By 10 K, the field-swept ESE spectrum displays essentially no contribution from the fast-relaxing $I_4$ species, as evidenced by the lack of characteristic features at the $g_1$ and $g_3$ turning points (Figure S10A, insets), and $T_1$ relaxation data collected at this temperature were excluded. The Curie behavior of $I_4$ was also investigated by plotting the spectral intensity against the inverse of temperature (Figure S11D,E). Intensities were obtained from either X-band CW or Q-band ESE data at the indicated turning points (Figure S10), and a scalar multiplier of $1 \times 10^7$ was applied to CW data to normalize intensity values between the two techniques. Additional scaling of the data was not necessary to obtain good agreement between the resultant linear fits on datasets collected at different frequencies.

While the $I_4$ ESE signal intensity drops off quickly as temperature is increased, the spectral contributions from additional (slower relaxing) species (e.g., $I_3$, residual $Mn^{II}$) also become more prevalent (Figure S10).[32] The ability to select only the fast component of the $T_1$ relaxation data for analysis underscores the benefit of the pulsed approach as a more selective probe for the $I_4$ species than simple measurement of the signal intensity. The presence of these underlying contributions to the absorption profile is evident in $T_1$ relaxation data collected at the $g_1$ turning point, where $\ln(1/\tau_1)$ values extracted at temperatures above 5.9 K no longer display a linear relationship with temperature (Figure S11B). This can be rationalized by considering the disparity in absolute signal intensity present at $g_1$ and $g_3$ (Figure S10B), where the stronger overall signal at the latter turning point provides better resolution of the $I_4$ contribution to inversion recovery data as temperature is increased.

**EPR Data Processing and Projected Basis Spin Hamiltonian (SH) Simulations.** Contaminating $Mn^{II}$ signals were removed from the $I_4$ EPR spectra at all three frequencies by subtraction of $Mn^{II}$-only reconstituted WT R2lox, collected under approximately the same conditions (Figure S31). Spectra were corrected for the baseline signal by a spline using Igor Pro (Wavemetrics, Lake Oswego, OR) data analysis software.

Small amounts of signals from matrix protons are still expected in $D_2O$ samples due to the presence of 20% glycerol ($C_3H_8O_3$; Fisher-Scientific) in pulsed EPR samples. Adjusting for density (glycerol density = 1.25 g/mL), the initial molar concentration of glycerol is 13.57 M. This is equivalent to 40.71 M exchangeable $^1H$ (three protons per glycerol molecule). A $D_2O$ sample including 20% glycerol will therefore also contain 8.14 M protons, due to exchange from the glycerol molecules. This amounts to ∼15% of the available $^1H/^2H$ in solution. While $^1H$ EDNMR collected on $D_2O$ samples are similar to $^1H$ EDNMR of $H_2O$ samples (Figure S32), comparison of signal intensities shows the $^1H$ signal in $D_2O$ samples is approximately 10−15× lower than observed in the $H_2O$ samples, within the level expected due to the presence of protiated glycerol in the prepared samples.

All EPR spectral simulations were carried out using the EasySpin toolbox within Matlab (R2019A).[48] Simulations performed in the projected basis were performed on an effective $S = {}^1/_2$ ground spin state for the projected hyperfine and g-tensor values within the following spin Hamiltonian (eq 2):

$$\hat{H} = \hat{H}_{\text{electron}} + \hat{H}_{M_i} + \hat{H}_{\text{ligand}} \quad (2)$$

where the three components are

$$\hat{H}_{\text{electron}} = \beta\vec{H}\cdot\hat{g}\cdot\vec{S_T},$$

$$\hat{H}_{M_i} = \sum_i \left(-\beta_M g_M \vec{H}\cdot\vec{I_M} + \vec{S_T}\cdot\hat{A}_i\cdot\vec{I_i} + \vec{I_i}\cdot\hat{Q}_i\cdot\vec{I_i}\right),$$

$$\hat{H}_{\text{ligand}} = \sum_i \left(-\beta_L g_L \vec{H}\cdot\vec{I_L} + \vec{S_T}\cdot\hat{A}_L\cdot\vec{I_L} + \vec{I_L}\cdot\hat{Q}_L\cdot\vec{I_L}\right).$$

encompassing the Zeeman term for the total electron spin, the Zeeman terms for the metals (M) and ligand (L) nuclei, the hyperfine (A) terms, and the quadrupolar (Q) terms.

CW and pulsed ESE simulations were carried out using the EasySpin core function pepper. Simulations included a linewidth of 1.5 mT (2 mT for W-band). H-strain was included for all CW spectra at $[H_1, H_2, H_3] = [80, 100, 130]$ MHz; Q- and W-band data included g-strain of $[B_1, B_2, B_3] = [0.006, 0.001, -0.003]$ and A-strain of $[A_1, A_2, A_3] = [30, 120, 100]$ MHz at Q-band or $[A_1, A_2, A_3] = [100, 0, 0]$ at W-band. ESEEM and HYSCORE simulations were performed using the EasySpin core function saffron.[47] Time-domain three-pulsed ESEEM data was subjected to subtraction of the exponential decay, application of a hamming window, zero-filling, and then a cross-term averaged fast Fourier transform. A satisfactory fit to the $^{14}N$ ESEEM and HYSCORE data could not be achieved without inclusion of Euler angles to rotate the hyperfine and quadrupole tensors with respect to the g-tensor (Figure S33). Euler angles were applied through the zyz convention. Errors on the $I_3$ and $I_4$ g- and $^{55}Mn$ hyperfine tensor values were obtained by varying each of the simulation parameters individually until visually unsatisfactory fits were obtained (Table 1 and Figures S34 and S35).[94,95]

**Extraction of Full SH Parameters.** Direct simulation of the experimental spectra in the projected $S_T = {}^1/_2$ basis was used to obtain the projected hyperfine tensors on each metal site and projected g-tensor of the coupled system. As temperature-dependent relaxation studies failed to provide a reliable $J$ value due to the magnitude of coupling and possible contributions from other relaxation pathways, simulations of the experimental spectra were performed in the intrinsic basis to further resolve $J$ and D. The general spin Hamiltonian describing an exchange-coupled system can be written as (eq 3)

$$\hat{H} = \hat{H}_{\text{Fe(III)}} + \hat{H}_{\text{Mn(III)}} + \hat{H}_{\text{ex}} \quad (3)$$

where the Hamiltonian associated with each site $I$ (intrinsic Hamiltonian) is (eq 4)

$$\hat{H}_i = \vec{S_i}\cdot\hat{D}_i\cdot\vec{S_i} + \beta\vec{H}\cdot\hat{g}_i\cdot\vec{S_i}, \quad (4)$$

and $\hat{H}_{\text{ex}}$ is reflected by the Heisenberg−Dirac−von Vleck Hamiltonian (eq 5):


https://doi.org/10.1021/jacs.1c13738
J. Am. Chem. Soc. 2022, 144, 11991−12006

$$\hat{H}_{ex} = -2J \overrightarrow{S_{Mn}} \overrightarrow{S_{Fe}}, \quad (5)$$

The effective g-tensor G with the principal components is related to on-site SH parameters through the spin-projection coefficients $\rho$ (eq 6):

$$G = \rho_1 g_1 + \rho_2 g_2 + \frac{\rho_1 \rho_2}{5J}(g_1 - g_2)[(3\rho_1 + 1)D_1 - (3\rho_2 + 1)D_2] \quad (6)$$

where $\rho$ is the isotropic spin projection factor and defined as the ratio of the on-site spin of the subspace to the total spin of the coupled system (eq 7):

$$\rho_i = \frac{S_i(S_i + 1) - S_j(S_j + 1) + S_{total}(S_{total} + 1)}{2S_{total}(S_{total} + 1)} \quad (7)$$

which gives $\rho_{Mn(III)} = -\frac{4}{3}$, and $\rho_{Fe(III)} = \frac{7}{3}$. In the strong coupling limits, the projected G and $A_i$ are given as (eqs 8 and 9)

$$G = \rho_1 g_1 + \rho_2 g_2 \quad (8)$$

$$A = \rho_1 a_1 + \rho_2 a_2 \quad (9)$$

The intrinsic g, D, and E/D values of the isotropic, high-spin Fe(III) were set to 2, 0, and 0, respectively, and those of the high-spin Mn(III) site were set to [2, 1.99, 1.98] due to the smaller $S_i$ and Jahn–Teller distortion.[44] Initial guesses for the Mn(III) on-site parameters were estimated following the procedures laid out by Guigliarelli et al.[46] and Que et al.[45] to calculate the projected g-values as a function of $D_i$, $E_i/D$, and $J$. To constrain the estimated values of D, E, and J, the calculated principal g-tensors were considered close enough to experimental values with an absolute error threshold of 2.6 $\times 10^{-2}$.

The intrinsic parameters were further refined through EPR spectral simulations using the EasySpin Toolbox with the core function pepper. The projected SH parameters provided target values, and the EPR spectrum was simulated within the full spin Hamiltonian model to obtain the intrinsic g-values, J, D, E/D, and a on each metal site. The calculated intrinsic hyperfine tensors from calculation were used as a simulation starting point with the assumptions of an isotropic Fe(III) site and an axial Mn(III) site. The effect of isotopic substitution was examined by changing only the value of the exchange coupling $J$ to account for the differences in projected values. The rhombicity of the $Mn^{III}$ ZFS tensor was not able to be resolved from these simulations; we present the fully axial case in the main text in the interest of reducing the number of assigned variables given the limited experimental information available.

**Density Functional Theory (DFT) Calculations.** All calculations used the ORCA quantum chemistry software package v4.2.1.[96]

**Model Construction.** Computational models of $I_4$ were developed starting from the R2lox crystal structure (4HR0).[9] The bridging fatty acid was removed. Residues that coordinate to the metals (E69, H105, E102, H205, E202) as well as Y175 in the secondary sphere were kept in their entirety. Side chains were truncated at the amide bond by H-termination to retain charge neutrality, and hydrogens were added. Computational models of $I_3$ were developed starting from the G68L Fe/Fe R2lox crystal structure (6I93),[37] following the same procedure as $I_4$ model construction with inclusion of the D201 residue.

**Geometry Optimization.** DFT calculations used the unrestricted formalism and hybrid TPSSh functional, along with zeroth-order regular approximation (ZORA) to account for the relativistic approximation[97−99] and the D3 dispersion method. Def2-TZVP(-f) basis sets were used with RIJCOSX approximation. Tight SCF, SlowConv criteria, and increased integration grids (grid6 and grid6X) were applied. Positions of hydrogen atoms were optimized followed by the geometry optimization of the whole active site in the high spin state with Cartesian constraints on the $\alpha$-carbons and the aryl group of Y175. Atoms are numbered as given in Figure S36.

**Frontier Molecular Orbital Visualization.** Frontier molecular orbitals (FMOs) that are localized on the metals of selected models were visualized using the orca_plot program on the localized unrestricted natural orbitals (Figure S37). Energies of the MOs were obtained from the quasi-restricted transformation.[67]

**Spectroscopic Properties.** Single-point calculations were used to assess properties of the ground state configurations. Sample input files for each type of calculation are given in the SI.

The exchange coupling constants ($J$) as well as the hyperfine tensors (A) for both metal cofactors were calculated within the broken-symmetry (BS) formalism. Theoretical ZFS parameters of the Mn(III) site were obtained by substituting Fe(III) with diamagnetic Ga(III).

The intrinsic hyperfine tensors $A_{iso,\ site}$ were calibrated according to previous studies (eq 10):[98]

$$a_{site}^{(i,j)} = A_{BS}^{j} \frac{\langle S_z \rangle_{BS}}{S_i} \quad (10)$$

where $S_i$ is the site spin number of subsystem $i$, $\langle S_z \rangle_{BS}$ is the total spin number of the BS system (i.e., $^1/_2$), and $A_{BS}^{j}$is the hyperfine tensor calculated directly from BS-DFT for nucleus $j$. A scaling factor $f = 1.5$ was applied as a calibration factor for the calculated-to-experimental conversion.[20,59,96,100]

The exchange coupling constant $J$ between the two metal sites was calculated based on the Heisenberg–Dirac–von Vleck Hamiltonian (eq 11):

$$\hat{H} = -2J \overrightarrow{S_{Mn}} \overrightarrow{S_{Fe}} \quad (11)$$

For the BS approach, the direct exchange coupling constant $J$ was calculated using the Yamaguchi method implemented in ORCA (eq 12):[96]

$$J = -\frac{E_{HS} - E_{BS}}{\langle S^2 \rangle_{HS} - \langle S^2 \rangle_{BS}}, \quad (12)$$

For establishing a correlation between $J$ and the hydroxyl O–H length/hydrogen bonding (Figure S28), the O–H bond length of the bridging hydroxide ligand in the model complex 2 ($H_2O$-$Mn^{III}$-$\mu$OH-$Fe^{III}$) was scanned from 1.0 to 1.3 Å in increments of 0.028 Å, and the corresponding exchange coupling constant $J$ was calculated at each geometry.

## ■ ASSOCIATED CONTENT

### Supporting Information

The Supporting Information is available free of charge at https://pubs.acs.org/doi/10.1021/jacs.1c13738.

Supplemental simulations, power and temperature-dependent fits, additional spectroscopic data, control samples, error analysis, optimized geometries of DFT models, structural and spectroscopic metrics, sample calculation input files (PDF)

## ■ AUTHOR INFORMATION


### Corresponding Author

**Hannah S. Shafaat** − *The Ohio State Biochemistry Program and Department of Chemistry and Biochemistry, The Ohio State University, Columbus, Ohio 43210, United States;* orcid.org/0000-0003-0793-4650; Email: shafaat.1@osu.edu

### Authors

**Effie C. Kisgeropoulos** − *The Ohio State Biochemistry Program, The Ohio State University, Columbus, Ohio 43210, United States;* orcid.org/0000-0003-1842-5691

**Yunqiao J. Gan** − *Department of Chemistry and Biochemistry, The Ohio State University, Columbus, Ohio 43210, United States;* orcid.org/0000-0002-6391-4286
**Samuel M. Greer** − *National High Magnetic Field Laboratory, Florida State University, Tallahassee, Florida 32310, United States; Department of Chemistry and Biochemistry, Florida State University, Tallahassee, Florida 32306, United States;* orcid.org/0000-0001-8225-3252
**Joseph M. Hazel** − *Department of Chemistry and Biochemistry, The Ohio State University, Columbus, Ohio 43210, United States*

Complete contact information is available at: https://pubs.acs.org/10.1021/jacs.1c13738

### Author Contributions

‖E.C.K. and Y.J.G. contributed equally to this work

### Notes

The authors declare no competing financial interest.

## ■ ACKNOWLEDGMENTS

H.S.S. would like to acknowledge support from the NIH National Institute for General Medical Sciences (R35 GM128852). Part of this work was performed at the National High Magnetic Field Laboratory (NHMFL), which is supported by NSF Cooperative Agreement No. DMR-1644779 and the State of Florida. E.C.K. would like to acknowledge partial support from a Pelotonia Graduate Fellowship. J.M.H. would like to acknowledge support from the NIH National Institute for General Medical Sciences Molecular Biophysics Training Grant (T32 GM118291). The authors gratefully acknowledge Professor Stephen Hill (FSU, NHMFL), Dr. Likai Song (NHMFL), and Dr. Krishnendu Kundu (NHMFL) for assistance with collecting data at the NHMFL and for helpful discussions. The authors would like to acknowledge Professor Gary Lorigan (Miami University; MU) and Dr. Robert McCarrick (MU) for assistance with collecting pulsed X- and Q-band data at the Advanced EPR Facility at Miami University, which was supported by NSF MRI 0722403 and NSF MRI 1725502. The authors would also like to acknowledge Professor Joshua Telser (Roosevelt University) for helpful discussions about isotope-dependent $Mn^{III}$ spin Hamiltonian parameters.

## ■ REFERENCES

(1) Jasniewski, A. J.; Que, L., Jr. Dioxygen Activation by Nonheme Diiron Enzymes: Diverse Dioxygen Adducts, High-Valent Intermediates, and Related Model Complexes. *Chem. Rev.* **2018**, *118*, 2554−2592.
(2) Wang, V. C.-C.; Maji, S.; Chen, P. P.-Y.; Lee, H. K.; Yu, S. S.-F.; Chan, S. I. Alkane Oxidation: Methane Monooxygenases, Related Enzymes, and Their Biomimetics. *Chem. Rev.* **2017**, *117*, 8574−8621.
(3) Mathevon, C.; Pierrel, F.; Oddou, J.-L.; Garcia-Serres, R.; Blondin, G.; Latour, J.-M.; Ménage, S.; Gambarelli, S.; Fontecave, M.; Atta, M. tRNA-modifying MiaE protein from Salmonella typhimurium is a nonheme diiron monooxygenase. *Proc. Natl. Acad. Sci. U. S. A.* **2007**, *104*, 13295−13300.
(4) Li, N.; Nørgaard, H.; Warui, D. M.; Booker, S. J.; Krebs, C.; Bollinger, J. M., Jr. Conversion of Fatty Aldehydes to Alka(e)nes and Formate by a Cyanobacterial Aldehyde Decarbonylase: Cryptic Redox by an Unusual Dimetal Oxygenase. *J. Am. Chem. Soc.* **2011**, *133*, 6158−6161.
(5) Warui, D. M.; Li, N.; Nørgaard, H.; Krebs, C.; Bollinger, J. M., Jr.; Booker, S. J. Detection of Formate, Rather than Carbon Monoxide, As the Stoichiometric Coproduct in Conversion of Fatty Aldehydes to Alkanes by a Cyanobacterial Aldehyde Decarbonylase. *J. Am. Chem. Soc.* **2011**, *133*, 3316−3319.
(6) Jiang, W.; Yun, D.; Saleh, L.; Barr, E. W.; Xing, G.; Hoffart, L. M.; Maslak, M.-A.; Krebs, C.; Bollinger, J. M., Jr. A manganese(IV)/iron(III) cofactor in Chlamydia trachomatis ribonucleotide reductase. *Science* **2007**, *316*, 1188−1191.
(7) Voevodskaya, N.; Lendzian, F.; Ehrenberg, A.; Gräslund, A. High catalytic activity achieved with a mixed manganese-iron site in protein R2 of Chlamydia ribonucleotide reductase. *FEBS Lett.* **2007**, *581*, 3351−3355.
(8) Andersson, C. S.; Högbom, M. A Mycobacterium tuberculosis ligand-binding Mn/Fe protein reveals a new cofactor in a remodeled R2-protein scaffold. *Proc. Natl. Acad. Sci.* **2009**, *106*, 5633−5638.
(9) Griese, J. J.; Roos, K.; Cox, N.; Shafaat, H. S.; Branca, R. M. M.; Lehtiö, J.; Gräslund, A.; Lubitz, W.; Siegbahn, P. E. M.; Högbom, M. Direct observation of structurally encoded metal discrimination and ether bond formation in a heterodinuclear metalloprotein. *Proc. Natl. Acad. Sci. U. S. A.* **2013**, *110*, 17189−17194.
(10) Irving, H.; Williams, R. J. P. The Stability of Transition-Metal Complexes. *J. Chem. Soc.* **1953**, *0*, 3192−3210.
(11) Kisgeropoulos, E. C.; Griese, J. J.; Smith, Z. R.; Branca, R. M. M.; Schneider, C. R.; Högbom, M.; Shafaat, H. S. Key Structural Motifs Balance Metal Binding and Oxidative Reactivity in a Heterobimetallic Mn/Fe Protein. *J. Am. Chem. Soc.* **2020**, *142*, 5338−5354.
(12) Kutin, Y.; Srinivas, V.; Fritz, M.; Kositzki, R.; Shafaat, H. S.; Birrell, J.; Bill, E.; Haumann, M.; Lubitz, W.; Högbom, M. Divergent assembly mechanisms of the manganese/iron cofactors in R2lox and R2c proteins. *J. Inorg. Biochem.* **2016**, *162*, 164−177.
(13) Dassama, L. M. K.; Krebs, C.; Bollinger, J. M., Jr.; Rosenzweig, A. C.; Boal, A. K. Structural Basis for Assembly of the MnIV/FeIII Cofactor in the Class Ic Ribonucleotide Reductase from Chlamydia trachomatis. *Biochemistry* **2013**, *52*, 6424−6436.
(14) Bollinger, J. M., Jr.; Jiang, W.; Green, M. T.; Krebs, C. The manganese(IV)/iron(III) cofactor of Chlamydia trachomatis ribonucleotide reductase: structure, assembly, radical initiation, and evolution. *Curr. Opin. Struct. Biol.* **2008**, *18*, 650−657.
(15) Jiang, W.; Bollinger, J. M., Jr.; Krebs, C. The active form of Chlamydia trachomatis ribonucleotide reductase R2 protein contains a heterodinuclear Mn(IV)/Fe(III) cluster with S=1 ground state. *J. Am. Chem. Soc.* **2007**, *129*, 7504−7505.
(16) Jiang, W.; Hoffart, L. M.; Krebs, C.; Bollinger, J. M., Jr. A Manganese(IV)/Iron(IV) Intermediate in Assembly of the Manganese(IV)/Iron(III) Cofactor of Chlamydia trachomatis Ribonucleotide Reductase. *Biochemistry* **2007**, *46*, 8709−8716.
(17) Dassama, L. M. K.; Jiang, W.; Varano, P. T.; Pandelia, M.-E.; Conner, D. A.; Xie, J.; Bollinger, J. M., Jr.; Krebs, C. Radical-Translocation Intermediates and Hurdling of Pathway Defects in "Super-oxidized" ($Mn^{IV}/Fe^{IV}$) Chlamydia trachomatis Ribonucleotide Reductase. *J. Am. Chem. Soc.* **2012**, *134*, 20498−20506.
(18) Griese, J. J.; Branca, R. M. M.; Srinivas, V.; Högbom, M. Ether cross-link formation in the R2-like ligand-binding oxidase. *J. Biol. Inorg. Chem.* **2018**, 879−886.
(19) Maugeri, P. T.; Griese, J. J.; Branca, R. M.; Miller, E. K.; Smith, Z. R.; Eirich, J.; Högbom, M.; Shafaat, H. S. Driving Protein Conformational Changes with Light: Photoinduced Structural Rearrangement in a Heterobimetallic Oxidase. *J. Am. Chem. Soc.* **2018**, *140*, 1471−1480.
(20) Shafaat, H. S.; Griese, J. J.; Pantazis, D. A.; Roos, K.; Andersson, C. S.; Popović-Bijelić, A.; Gräslund, A.; Siegbahn, P. E. M.; Neese, F.; Lubitz, W. Electronic Structural Flexibility of Heterobimetallic Mn/Fe Cofactors: R2lox and R2c Proteins. *J. Am. Chem. Soc.* **2014**, *136*, 13399−13409.
(21) Griese, J. J.; Kositzki, R.; Schrapers, P.; Branca, R. M. M.; Nordström, A.; Lehtiö, J.; Haumann, M.; Högbom, M. Structural Basis for Oxygen Activation at a Heterodinuclear Manganese/Iron Cofactor. *J. Biol. Chem.* **2015**, *290*, 25254−25272.
(22) Högbom, M.; Stenmark, P.; Voevodskaya, N.; McClarty, G.; Gräslund, A.; Nordlund, P. The radical site in chlamydial

ribonucleotide reductase defines a new R2 subclass. *Science* **2004**, *305*, 245−248.
(23) Murray, L. J.; Lippard, S. J. Substrate Trafficking and Dioxygen Activation in Bacterial Multicomponent Monooxygenases. *Acc. Chem. Res.* **2007**, *40*, 466−474.
(24) Merkx, M.; Kopp, D. A.; Sazinsky, M. H.; Blazyk, J. L.; Müller, J.; Lippard, S. J. Dioxygen Activation and Methane Hydroxylation by Soluble Methane Monooxygenase: A Tale of Two Irons and Three Proteins. *Angew. Chem., Int. Ed.* **2001**, *40*, 2782−2807.
(25) DeRose, V. J.; Liu, K. E.; Kurtz, D. M., Jr.; Hoffman, B. M.; Lippard, S. J. Proton ENDOR identification of bridging hydroxide ligands in mixed-valent diiron centers of proteins: methane monooxygenase and semimet azidohemerythrin. *J. Am. Chem. Soc.* **1993**, *115*, 6440−6441.
(26) DeRose, V. J.; Liu, K. E.; Lippard, S. J.; Hoffman, B. M. Investigation of the Dinuclear Fe Center of Methane Monooxygenase by Advanced Paramagnetic Resonance Techniques: On the Geometry of DMSO Binding. *J. Am. Chem. Soc.* **1996**, *118*, 121−134.
(27) Davydov, R.; Kuprin, S.; Graeslund, A.; Ehrenberg, A. Electron Paramagnetic Resonance Study of the Mixed-Valent Diiron Center in Escherichia coli Ribonucleotide Reductase Produced by Reduction of Radical-Free Protein R2 at 77 K. *J. Am. Chem. Soc.* **1994**, *116*, 11120−11128.
(28) Davydov, R.; Behrouzian, B.; Smoukov, S.; Stubbe, J.; Hoffman, B. M.; Shanklin, J. Effect of Substrate on the Diiron(III) Site in Stearoyl Acyl Carrier Protein Δ9-Desaturase as Disclosed by Cryoreduction Electron Paramagnetic Resonance/Electron Nuclear Double Resonance Spectroscopy. *Biochemistry* **2005**, *44*, 1309−1315.
(29) Cox, N.; Nalepa, A.; Pandelia, M.-E.; Lubitz, W.; Savitsky, A. Pulse Double-Resonance EPR Techniques for the Study of Metallobiomolecules. In *Methods in Enzymology*; Elsevier: 2015; Vol. *563*, pp. 211−249, DOI: 10.1016/bs.mie.2015.08.016.
(30) Bencini, A.; Gatteschi, D. *Electron paramagnetic resonance of exchange coupled systems*; Springer-Verlag New York, Inc.: Secaucus, New Jersey, USA; Berlin, West Germany. Illus; 1990.
(31) Stoll, S.; Shafaat, H. S.; Krzystek, J.; Ozarowski, A.; Tauber, M. J.; Kim, J. E.; Britt, R. D. Hydrogen Bonding of Tryptophan Radicals Revealed by EPR at 700 GHz. *J. Am. Chem. Soc.* **2011**, *133*, 18098−18101.
(32) Miller, E. K.; Trivelas, N. E.; Maugeri, P. T.; Blaesi, E. J.; Shafaat, H. S. Time-Resolved Investigations of Heterobimetallic Cofactor Assembly in R2lox Reveal Distinct Mn/Fe Intermediates. *Biochemistry* **2017**, *56*, 3369−3379.
(33) Högbom, M. The manganese/iron-carboxylate proteins: what is what, where are they, and what can the sequences tell us? *J. Biol. Inorg. Chem.* **2010**, *15*, 339−349.
(34) Schmidt, F.; Donahoe, S.; Hagens, K.; Mattow, J.; Schaible, U. E.; Kaufmann, S. H. E.; Aebersold, R.; Jungblut, P. R. Complementary Analysis of the Mycobacterium tuberculosis Proteome by Two-dimensional Electrophoresis and Isotope-coded Affinity Tag Technology. *Mol. Cell. Proteomics* **2004**, *3*, 24−42.
(35) Ehrt, S.; Rhee, K. Mycobacterium tuberculosis metabolism and host interaction: mysteries and paradoxes. *Pathog. Mycobact. Tuberc. Interact. Host Org.* **2013**, *374*, 163−188.
(36) Neyrolles, O.; Wolschendorf, F.; Mitra, A.; Niederweis, M. Mycobacteria, metals, and the macrophage. *Immunol. Rev.* **2015**, *264*, 249−263.
(37) Kutin, Y.; Kositzki, R.; Branca, R. M. M.; Srinivas, V.; Lundin, D.; Haumann, M.; Högbom, M.; Cox, N.; Griese, J. J. Chemical flexibility of heterobimetallic Mn/Fe cofactors: R2lox and R2c proteins. *J. Biol. Chem.* **2019**, *294*, 18372−18386.
(38) Jiang, W.; Xie, J.; Nørgaard, H.; Bollinger, J. M., Jr.; Krebs, C. Rapid and Quantitative Activation of Chlamydia trachomatis Ribonucleotide Reductase by Hydrogen Peroxide. *Biochemistry* **2008**, *47*, 4477−4483.
(39) Pace, R. J.; Smith, P.; Bramley, R.; Stehlik, D. EPR saturation and temperature dependence studies on signals from the oxygen-evolving centre of photosystem II. *Biochim. Biophys. Acta, Bioenerg.* **1991**, *1058*, 161−170.
(40) Smoukov, S. K.; Telser, J.; Bernat, B. A.; Rife, C. L.; Armstrong, R. N.; Hoffman, B. M. EPR Study of Substrate Binding to the Mn(II) Active Site of the Bacterial Antibiotic Resistance Enzyme FosA: A Better Way To Examine Mn(II). *J. Am. Chem. Soc.* **2002**, *124*, 2318−2326.
(41) Schweiger, A.; Jeschke, G. *Principles of Pulse Electron Paramagnetic Resonance*; Oxford University Press, 2001, Oxford, England.
(42) Maly, T.; Prisner, T. F. Relaxation filtered hyperfine spectroscopy (REFINE). *J. Magn. Reson.* **2004**, *170*, 88−96.
(43) Maly, T.; MacMillan, F.; Zwicker, K.; Kashani-Poor, N.; Brandt, U.; Prisner, T. F. Relaxation Filtered Hyperfine (REFINE) Spectroscopy: A Novel Tool for Studying Overlapping Biological Electron Paramagnetic Resonance Signals Applied to Mitochondrial Complex I. *Biochemistry* **2004**, *43*, 3969−3978.
(44) Cox, N.; Rapatskiy, L.; Su, J.-H.; Pantazis, D. A.; Sugiura, M.; Kulik, L.; Dorlet, P.; Rutherford, A. W.; Neese, F.; Boussac, A.; Lubitz, W.; Messinger, J. Effect of $Ca^{2+}/Sr^{2+}$ Substitution on the Electronic Structure of the Oxygen-Evolving Complex of Photosystem II: A Combined Multifrequency EPR, 55Mn-ENDOR, and DFT Study of the $S_2$ State. *J. Am. Chem. Soc.* **2011**, *133*, 3635−3648.
(45) Li, F.; Chakrabarti, M.; Dong, Y.; Kauffmann, K.; Bominaar, E. L.; Münck, E.; Que, L. Structural, EPR, and Mössbauer Characterization of (μ-Alkoxo)(μ-Carboxylato)Diiron(II,III) Model Complexes for the Active Sites of Mixed-Valent Diiron Enzymes. *Inorg. Chem.* **2012**, *51*, 2917−2929.
(46) Guigliarelli, B.; Bertrand, P.; Gayda, J.-P. Contribution of the fine structure terms to the g values of the biological Fe iii−Fe ii clusters. *J. Chem. Phys.* **1986**, *85*, 1689−1692.
(47) Stoll, S.; Britt, R. D. General and efficient simulation of pulse EPR spectra. *Phys. Chem. Chem. Phys.* **2009**, *11*, 6614−6625.
(48) Stoll, S.; Schweiger, A. EasySpin, a comprehensive software package for spectral simulation and analysis in EPR. *J. Magn. Reson.* **2006**, *178*, 42−55.
(49) Epel, B.; Schäfer, K.-O.; Quentmeier, A.; Friedrich, C.; Lubitz, W. Multifrequency EPR analysis of the dimanganese cluster of the putative sulfate thiohydrolase SoxB of Paracoccus pantotrophus. *J. Biol. Inorg. Chem.* **2005**, *10*, 636−642.
(50) Deligiannakis, Y.; Louloudi, M.; Hadjiliadis, N. Electron spin echo envelope modulation (ESEEM) spectroscopy as a tool to investigate the coordination environment of metal centers. *Coord. Chem. Rev.* **2000**, *204*, 1−112.
(51) Lee, H.-I.; Doan, P. E.; Hoffman, B. M. General Analysis of 14N (I = 1) Electron Spin Echo Envelope Modulation. *J. Magn. Reson.* **1999**, *140*, 91−107.
(52) Stich, T. A.; Whittaker, J. W.; Britt, R. D. Multifrequency EPR Studies of Manganese Catalases Provide a Complete Description of Protemaceous Nitrogen Coordination. *J. Phys. Chem. B* **2010**, *114*, 14178−14188.
(53) Stich, T. A.; Yeagle, G. J.; Service, R. J.; Debus, R. J.; Britt, R. D. Ligation of D1-His332 and D1-Asp170 to the Manganese Cluster of Photosystem II from Synechocystis Assessed by Multifrequency Pulse EPR Spectroscopy. *Biochemistry* **2011**, *50*, 7390−7404.
(54) Cox, N.; Lubitz, W.; Savitsky, A. W-band ELDOR-detected NMR (EDNMR) spectroscopy as a versatile technique for the characterisation of transition metal−ligand interactions. *Mol. Phys.* **2013**, *111*, 2788−2808.
(55) Cox, N.; Nalepa, A.; Lubitz, W.; Savitsky, A. ELDOR-detected NMR: A general and robust method for electron-nuclear hyperfine spectroscopy? *J. Magn. Reson.* **2017**, *280*, 63−78.
(56) Rapatskiy, L.; Ames, W. M.; Pérez-Navarro, M.; Savitsky, A.; Griese, J. J.; Weyhermüller, T.; Shafaat, H. S.; Högbom, M.; Neese, F.; Pantazis, D. A.; Cox, N. Characterization of Oxygen Bridged Manganese Model Complexes Using Multifrequency 17O-Hyperfine EPR Spectroscopies and Density Functional Theory. *J. Phys. Chem. B* **2015**, *119*, 13904−13921.
(57) Cruickshank, P. A. S.; Bolton, D. R.; Robertson, D. A.; Hunter, R. I.; Wylde, R. J.; Smith, G. M. A kilowatt pulsed 94 GHz electron paramagnetic resonance spectrometer with high concentration

sensitivity, high instantaneous bandwidth, and low dead time. *Rev. Sci. Instrum.* **2009**, *80*, 103102.
(58) Beal, N. J.; Corry, T. A.; O'Malley, P. J. Comparison between Experimental and Broken Symmetry Density Functional Theory (BS-DFT) Calculated Electron Paramagnetic Resonance (EPR) Parameters of the $S_2$ State of the Oxygen-Evolving Complex of Photosystem II in Its Native (Calcium) and Strontium-Substituted Form. *J. Phys. Chem. B* **2017**, *121*, 11273−11283.
(59) Cox, N.; Ames, W.; Epel, B.; Kulik, L. V.; Rapatskiy, L.; Neese, F.; Messinger, J.; Wieghardt, K.; Lubitz, W. Electronic Structure of a Weakly Antiferromagnetically Coupled $Mn^{II}Mn^{III}$ Model Relevant to Manganese Proteins: A Combined EPR, $^{55}$Mn-ENDOR, and DFT Study. *Inorg. Chem.* **2011**, *50*, 8238−8251.
(60) Ames, W.; Pantazis, D. A.; Krewald, V.; Cox, N.; Messinger, J.; Lubitz, W.; Neese, F. Theoretical Evaluation of Structural Models of the $S_2$ State in the Oxygen Evolving Complex of Photosystem II: Protonation States and Magnetic Interactions. *J. Am. Chem. Soc.* **2011**, *133*, 19743−19757.
(61) Lohmiller, T.; Krewald, V.; Sedoud, A.; Rutherford, A. W.; Neese, F.; Lubitz, W.; Pantazis, D. A.; Cox, N. The First State in the Catalytic Cycle of the Water-Oxidizing Enzyme: Identification of a Water-Derived $\mu$-Hydroxo Bridge. *J. Am. Chem. Soc.* **2017**, *139*, 14412−14424.
(62) Tinberg, C. E.; Lippard, S. J. Dioxygen Activation in Soluble Methane Monooxygenase. *Acc. Chem. Res.* **2011**, *44*, 280−288.
(63) Jasniewski, A. J.; Knoot, C. J.; Lipscomb, J. D.; Que, L., Jr. A Carboxylate Shift Regulates Dioxygen Activation by the Diiron Nonheme $\beta$-Hydroxylase CmlA upon Binding of a Substrate-Loaded Nonribosomal Peptide Synthetase. *Biochemistry* **2016**, *55*, 5818−5831.
(64) Frisch, J. R.; McDonnell, R.; Rybak-Akimova, E. V.; Que, L., Jr. Factors Affecting the Carboxylate Shift Upon Formation of Nonheme Diiron-$O_2$ Adducts. *Inorg. Chem.* **2013**, *52*, 2627−2636.
(65) Spiller, N.; Bjornsson, R.; DeBeer, S.; Neese, F. Carbon Monoxide Binding to the Iron−Molybdenum Cofactor of Nitrogenase: a Detailed Quantum Mechanics/Molecular Mechanics Investigation. *Inorg. Chem.* **2021**, *60*, 18031−18047.
(66) Chilkuri, V. G.; DeBeer, S.; Neese, F. Ligand Field Theory and Angular Overlap Model Based Analysis of the Electronic Structure of Homovalent Iron−Sulfur Dimers. *Inorg. Chem.* **2020**, *59*, 984−995.
(67) Neese, F. Importance of Direct Spin−Spin Coupling and Spin-Flip Excitations for the Zero-Field Splittings of Transition Metal Complexes: A Case Study. *J. Am. Chem. Soc.* **2006**, *128*, 10213−10222.
(68) Abrams, M. L.; Sherrill, C. D. Natural orbitals as substitutes for optimized orbitals in complete active space wavefunctions. *Chem. Phys. Lett.* **2004**, *395*, 227−232.
(69) Campbell, K. A.; Force, D. A.; Nixon, P. J.; Dole, F.; Diner, B. A.; Britt, R. D. Dual-Mode EPR Detects the Initial Intermediate in Photoassembly of the Photosystem II Mn Cluster: The Influence of Amino Acid Residue 170 of the D1 Polypeptide on Mn Coordination. *J. Am. Chem. Soc.* **2000**, *122*, 3754−3761.
(70) Campbell, K. A.; Lashley, M. R.; Wyatt, J. K.; Nantz, M. H.; Britt, R. D. Dual-Mode EPR Study of Mn(III) Salen and the Mn(III) Salen-Catalyzed Epoxidation of cis-$\beta$-Methylstyrene. *J. Am. Chem. Soc.* **2001**, *123*, 5710−5719.
(71) Solomon, E. I.; Brunold, T. C.; Davis, M. I.; Kemsley, J. N.; Lee, S.-K.; Lehnert, N.; Neese, F.; Skulan, A. J.; Yang, Y.-S.; Zhou, J. Geometric and electronic structure/function correlations in non-heme iron enzymes. *Chem. Rev.* **2000**, *100*, 235−350.
(72) Bossek, U.; Weyhermüller, T.; Wieghardt, K.; Bonvoisin, J.; Girerd, J. J. Synthesis, E. S. R. spectrum and magnetic properties of a heterobinuclear complex containing the $\{Fe^{III}(\mu\text{-O})(\mu\text{-MeCO}_2)_2Mn^{III}\}^{2+}$ core. *J. Chem. Soc., Chem. Commun.* **1989**, *10*, 633−636.
(73) Crossland, P. M.; Guo, Y.; Que, L., Jr. Spontaneous Formation of an Fe/Mn Diamond Core: Models for the Fe/Mn Sites in Class 1c Ribonucleotide Reductases. *Inorg. Chem.* **2021**, 8710.
(74) Jiang, W.; Saleh, L.; Barr, E. W.; Xie, J.; Gardner, M. M.; Krebs, C.; Bollinger, J. M., Jr. Branched Activation- and Catalysis-Specific Pathways for Electron Relay to the Manganese/Iron Cofactor in Ribonucleotide Reductase from Chlamydia trachomatis. *Biochemistry* **2008**, *47*, 8477−8484.
(75) Kwak, Y.; Jiang, W.; Dassama, L. M. K.; Park, K.; Bell, C. B.; Liu, L. V.; Wong, S. D.; Saito, M.; Kobayashi, Y.; Kitao, S.; Seto, M.; Yoda, Y.; Alp, E. E.; Zhao, J.; Bollinger, J. M., Jr.; Krebs, C.; Solomon, E. I. Geometric and Electronic Structure of the Mn(IV)Fe(III) Cofactor in Class Ic Ribonucleotide Reductase: Correlation to the Class Ia Binuclear Non-Heme Iron Enzyme. *J. Am. Chem. Soc.* **2013**, *135*, 17573−17584.
(76) Doi, K.; McCracken, J.; Peisach, J.; Aisen, P. The binding of molybdate to uteroferrin. Hyperfine interactions of the binuclear center with 95Mo, 1H, and 2H. *J. Biol. Chem.* **1988**, *263*, 5757−5763.
(77) Willems, J.-P.; Lee, H.-I.; Burdi, D.; Doan, P. E.; Stubbe, J.; Hoffman, B. M. Identification of the protonated oxygenic ligands of ribonucleotide reductase intermediate X by Q-band $^{1,2}$H CW and pulsed ENDOR. *J. Am. Chem. Soc.* **1997**, *119*, 9816−9824.
(78) Soper, A. K.; Benmore, C. J. Quantum Differences between Heavy and Light Water. *Phys. Rev. Lett.* **2008**, *101*, No. 065502.
(79) McConnell, I. L.; Grigoryants, V. M.; Scholes, C. P.; Myers, W. K.; Chen, P.-Y.; Whittaker, J. W.; Brudvig, G. W. EPR−ENDOR Characterization of (17O, 1H, 2H) Water in Manganese Catalase and Its Relevance to the Oxygen-Evolving Complex of Photosystem II. *J. Am. Chem. Soc.* **2012**, *134*, 1504−1512.
(80) Beal, N. J.; O'Malley, P. J. Manganese Oxidation State Assignment for Manganese Catalase. *J. Am. Chem. Soc.* **2016**, *138*, 4358−4361.
(81) Suga, M.; Akita, F.; Yamashita, K.; Nakajima, Y.; Ueno, G.; Li, H.; Yamane, T.; Hirata, K.; Umena, Y.; Yonekura, S. An oxyl/oxo mechanism for oxygen-oxygen coupling in PSII revealed by an x-ray free-electron laser. *Science* **2019**, *366*, 334−338.
(82) Chrysina, M.; Heyno, E.; Kutin, Y.; Reus, M.; Nilsson, H.; Nowaczyk, M. M.; DeBeer, S.; Neese, F.; Messinger, J.; Lubitz, W.; Cox, N. Five-coordinate $Mn^{IV}$ intermediate in the activation of nature's water splitting cofactor. *Proc. Natl. Acad. Sci. U. S. A.* **2019**, *116*, 16841−16846.
(83) Kolling, D. R. J.; Samoilova, R. I.; Shubin, A. A.; Crofts, A. R.; Dikanov, S. A. Proton Environment of Reduced Rieske Iron−Sulfur Cluster Probed by Two-Dimensional ESEEM Spectroscopy. *J. Phys. Chem. A* **2009**, *113*, 653−667.
(84) Rose, K.; Shadle, S. E.; Eidsness, M. K.; Kurtz, D. M.; Scott, R. A.; Hedman, B.; Hodgson, K. O.; Solomon, E. I. Investigation of Iron−Sulfur Covalency in Rubredoxins and a Model System Using Sulfur K-Edge X-ray Absorption Spectroscopy. *J. Am. Chem. Soc.* **1998**, *120*, 10743−10747.
(85) Yeagle, G. J.; Gilchrist, M. L., Jr.; Walker, L. M.; Debus, R. J.; Britt, R. D. Multifrequency electron spin-echo envelope modulation studies of nitrogen ligation to the manganese cluster of photosystem II. *Philos. Trans. R. Soc., B* **2008**, *363*, 1157−1166.
(86) Lohmiller, T.; Krewald, V.; Navarro, M. P.; Retegan, M.; Rapatskiy, L.; Nowaczyk, M. M.; Boussac, A.; Neese, F.; Lubitz, W.; Pantazis, D. A.; Cox, N. Structure, ligands and substrate coordination of the oxygen-evolving complex of photosystem II in the $S_2$ state: a combined EPR and DFT study. *Phys. Chem. Chem. Phys.* **2014**, *16*, 11877−11892.
(87) Manley, O. M.; Fan, R.; Guo, Y.; Makris, T. M. Oxidative Decarboxylase UndA Utilizes a Dinuclear Iron Cofactor. *J. Am. Chem. Soc.* **2019**, *141*, 8684−8688.
(88) Zhang, B.; Rajakovich, L. J.; Van Cura, D.; Blaesi, E. J.; Mitchell, A. J.; Tysoe, C. R.; Zhu, X.; Streit, B. R.; Rui, Z.; Zhang, W. Substrate-Triggered Formation of a Peroxo-Fe2(III/III) Intermediate during Fatty Acid Decarboxylation by UndA. *J. Am. Chem. Soc.* **2019**, *141*, 14510−14514.
(89) Johnson, K. A. Chapter 23 Fitting Enzyme Kinetic Data with KinTek Global Kinetic Explorer. *Methods Enzymol.* **2009**, *467*, 601−626.

(90) Song, L.; Liu, Z.; Kaur, P.; Esquiaqui, J. M.; Hunter, R. I.; Hill, S.; Smith, G. M.; Fanucci, G. E. Toward increased concentration sensitivity for continuous wave EPR investigations of spin-labeled biological macromolecules at high fields. *J. Magn. Reson.* **2016**, *265*, 188−196.
(91) Eaton, G. R.; Eaton, S. S. Relaxation times of organic radicals and transition metal ions. In *Distance Measurements in Biological Systems by EPR*; Berliner, L. J.; Eaton, G. R.; Eaton, S. S., Eds.; Kluwer Academic Plenum Publishers: New York, New York, 2000; Vol. *19*, pp. 29−154.
(92) Eaton, G. R.; Eaton, S. S. Electron Paramagnetic Resonance Spectroscopy. In *Comprehensive Coordination Chemistry III*; Elsevier, 2021; pp. 44−59, DOI: 10.1016/B978-0-12-409547-2.14621-9.
(93) Kulik, L. V.; Lubitz, W.; Messinger, J. Electron Spin−Lattice Relaxation of the S0 State of the Oxygen-Evolving Complex in Photosystem II and of Dinuclear Manganese Model Complexes. *Biochemistry* **2005**, *44*, 9368−9374.
(94) Hayes, E. C.; Porter, T. R.; Barrows, C. J.; Kaminsky, W.; Mayer, J. M.; Stoll, S. Electronic Structure of a CuII−Alkoxide Complex Modeling Intermediates in Copper-Catalyzed Alcohol Oxidations. *J. Am. Chem. Soc.* **2016**, *138*, 4132−4145.
(95) Kisgeropoulos, E. C.; Manesis, A. C.; Shafaat, H. S. Ligand Field Inversion as a Mechanism to Gate Bioorganometallic Reactivity: Investigating a Biochemical Model of Acetyl CoA Synthase Using Spectroscopy and Computation. *J. Am. Chem. Soc.* **2021**, *143*, 849−867.
(96) Neese, F.; Wennmohs, F.; Becker, U.; Riplinger, C. The ORCA quantum chemistry program package. *J. Chem. Phys.* **2020**, *152*, 224108.
(97) van Wüllen, C. Molecular density functional calculations in the regular relativistic approximation: Method, application to coinage metal diatomics, hydrides, fluorides and chlorides, and comparison with first-order relativistic calculations. *J. Chem. Phys.* **1998**, *109*, 392−399.
(98) van Lenthe, E.; Ehlers, A.; Baerends, E.-J. Geometry optimizations in the zero order regular approximation for relativistic effects. *J. Chem. Phys.* **1999**, *110*, 8943−8953.
(99) van Lenthe, E.; Baerends, E. J.; Snijders, J. G. Relativistic Regular Two-Component Hamiltonians. *J. Chem. Phys.* **1993**, *99*, 4597−4610.
(100) Sinnecker, S.; Neese, F.; Noodleman, L.; Lubitz, W. Calculating the Electron Paramagnetic Resonance Parameters of Exchange Coupled Transition Metal Complexes Using Broken Symmetry Density Functional Theory: Application to a $Mn^{III}/Mn^{IV}$ Model Compound. *J. Am. Chem. Soc.* **2004**, *126*, 2613−2622.